

1 U-Pb dating on calcite paleosol nodules: first absolute age constraints 2 on the Miocene continental succession of the Paris Basin

3 Vincent Monchal¹, Rémi Rateau¹, Kerstin Drost¹, Cyril Gagnaison², Bastien Mennecart³, Renaud
4 Toullec², Koen Torremans⁴, David Chew¹

5 ¹Geology, School of Natural Sciences, Trinity College Dublin, Dublin, D02 PN40, Ireland

6 ²Département Géosciences, Unité Bassins-Réservoirs-Ressources (B2R-U2R 7511), Institut Polytechnique UniLaSalle
7 Beauvais, UniLaSalle-Université de Picardie, Beauvais, 30313, France

8 ³Naturhistorisches Museum Basel, Basel, 4001, Switzerland

9 ⁴ School of Earth Sciences, University College Dublin, Belfield, Dublin 4, Ireland

10 *Correspondence to:* Vincent Monchal (monchalv@tcd.ie)

11 Abstract

12 Continental sedimentary successions are typically less complete and more poorly preserved than the marine record, leading to
13 limited correlations between basins. Traditionally, intra-basin correlation employs radiometric dating of volcanic markers or
14 relative dating based on the fossil record. However, volcanic markers may not always be present, and biostratigraphy relies on
15 index fossils that are often sparse to absent in continental succession. Recent progress in carbonate U-Pb dating can improve
16 correlations between continental successions by providing absolute age constraints on carbonate deposition and/or on syn- to
17 post-depositional processes such as pedogenesis.

18 In this study, we analysed pedogenic calcite nodules within a continental Miocene succession in the southwestern Paris Basin
19 (the important paleontological site at Mauvières quarry, France). Following multimethod petrographic characterisation of the
20 samples, LA-ICP-MS U-Pb dating was employed to obtain formation ages on the pedogenic calcite nodules. The Tera-
21 Wasserburg intercept ages from five nodules from the same horizon ($19.3 \pm 1.3/1.4$ Ma, $18.8 \pm 2.7/2.7$ Ma, $19.11 \pm 0.84/0.94$ Ma,
22 $19.0 \pm 2.3/2.3$ Ma and $19.4 \pm 2.7/2.7$ Ma) are in excellent agreement with previous biostratigraphic constraints on the sequence.
23 Petrographic evidence points to a single crystallisation event, and we conclude that the formation of the calcite nodules
24 occurred at $19.22 \pm 0.66/0.79$ Ma (central age from a radial plot of the five Tera-Wasserburg intercept ages). This calcite
25 formation age is regarded to represent a minimum depositional age of the strata hosting the root nodules. It provides the first
26 absolute age for the continental Miocene succession (and Neogene mammal zone MN3) of the Paris Basin and allows
27 correlation with other continental basins independent of their fossil assemblages or where fossil content is absent.

29 **1 Introduction**

30 Biostratigraphy assigns relative ages to rock strata by using the fossil assemblages contained within them, with the goal of
31 showing that a particular horizon in a given section represents a similar period of time as an analogue horizon in a different
32 succession. It relies heavily on the presence of index fossils - fossils with a limited time range, wide geographic distribution,
33 and rapid evolutionary trends. The common absence of biostratigraphically-diagnostic index fossils in continental successions
34 is problematic, and absolute dating approaches often need to be applied to continental successions. Such approaches include
35 geochronology of volcanic horizons such as lava flows, ash beds, or cryptotephra (e.g., Rubidge et al., 2013; Smith et al.,
36 2017; Poujol et al., 2023), astronomic calibration (e.g., Kerr 1992, Montano et al., 2021), and magnetostratigraphic correlation
37 (e.g., Kalin and Kempf 2009). While volcanic horizons can provide accurate and precise absolute ages, they are not ubiquitous
38 in the sedimentary record. Carbonates are very common in terrestrial successions (except in humid climates) where they can
39 be classified as pedogenic or non-pedogenic, depending on whether they have formed by soil-forming processes (Zamanian et
40 al., 2016). Pedogenic carbonates comprise calcretes and dolocretes - paleosols that have been indurated by a pervasive calcitic
41 cement; pisoliths - globular nodules made of concentric calcitic spheres; and more generic calcitic nodules - indurated
42 concretions with a globular or cylindrical shape, often associated with calcitic cementation around plant roots (rhizocretions;
43 Zamanian et al., 2016).

44 The formation of carbonates nodules can be classified according to the morphology of the nodule and the postulated fluid
45 pathway that led to the formation of the nodule (Zamanian et al., 2016). *Perdescendum* models and *Perascendum* models
46 involve dissolution of carbonate with reprecipitation in a different horizon (a deeper horizon for *Perdescendum* and shallower
47 for *Perascendum*) while *in situ* models do not imply significant carbonate migration through the soil profile (Zamanian et al.,
48 2016). Biological models invoke absorption of Ca-enriched fluid by an organism, leading to calcification of Ca-bearing organs
49 or supersaturation that induces carbonate precipitation (Zamanian et al., 2016). These biological models include rhizolith
50 formation, whereby plant roots pump the water from Ca-enriched fluids leaving behind residual Ca^{2+} ions that react with the
51 CO_2 emitted by rhizomicrobial respiration, resulting in the earliest carbonate cements around the root (Zamanian et al., 2016).
52 After the root dies, the void created is filled (partially to completely) by calcite resulting from the activity of bacteria, algae,
53 or by dissolution of the early carbonate cement and reprecipitation into cavities (Aguirre Palafox et al., 2024). When burial,
54 compaction starts, intergranular space and compaction cracks can create new cavities for carbonate precipitation. With burial,
55 the nodule can travel from the oxidising conditions of the vadose zone towards the more reducing environment of the phreatic
56 zone (Aguirre Palafox et al., 2024). This results in chemical changes (e.g. in Fe, Mn, and Pb) observable in
57 cathodoluminescence (CL) images but which also affect U-Pb geochronology (Aguirre Palafox et al., 2024).
58 U-Pb dating of calcium carbonate started in the late 1980s using isotope dilution (ID) – thermal ionisation mass spectrometry
59 (TIMS) methods (Smith and Farquhar, 1989; Roberts et al., 2020 and references therein). Most terrestrial U-Pb carbonate
60 dating studies have focused on non-pedogenic carbonates (e.g. speleothems, tufas, and lacustrine carbonates; see review in
61 Rasbury and Cole, 2009 and a more recent review by Rasbury et al., 2023). The first U-Pb dating studies applied to terrestrial

62 pedogenic carbonates took place in the mid-1990s on Paleozoic uranium-rich dolocretes, developed subaerially on top of
63 marine limestones (Hoff et al., 1995; Winter and Johnson, 1995). Over the following years, a series of ID-TIMS U-Pb dating
64 studies yielded meaningful subaerial exposure ages from 1) Late Paleozoic paleosol-derived sparry calcite developed on top
65 of marine carbonate cycloths in the southwestern USA (Rasbury et al., 1997, 1998, 2000; Rasbury and Cole, 2009); 2) Late
66 Paleozoic dolocretes from Kansas, USA (Luczaj and Goldstein, 2000); 3) Late Paleozoic subaerially soil-modified palustrine
67 limestones in Ohio, USA (Becker et al., 2001); and 4) Triassic calcretes developed on top of fluvial siliciclastics deposits in
68 Connecticut, USA (Wang et al., 1998) (Table 1).

69 Since the mid-2010s, advances in laser ablation inductively coupled plasma mass spectrometry (LA-ICP-MS) have allowed
70 U-Pb dating of carbonates with the benefits of much greater spatial resolution, mineralogical context (being in-situ), and
71 sample throughput (e.g., Li et al., 2014; Roberts and Walker, 2016; Nuriel et al., 2017). While individual LA-ICP-MS spot
72 ablation U-Pb data are typically significantly less precise than ID-TIMS U-Pb analyses, the high spatial resolution of the
73 approach means it can commonly encounter both high and low U/Pb portions of the sample, resulting in age regressions with
74 superior precision compared to ID-TIMS U-Pb dating studies which employ bulk sampling (e.g., Li et al., 2014; Roberts et
75 al., 2020). The technique has been employed to date pedogenesis including 1) Eocene pedogenic calcite nodules from Montana,
76 USA (Methner et al., 2016), 2) an Upper Triassic continental succession with calcite nodules and interbedded volcanic markers
77 from Argentina (Aguirre Palafox et al., 2024), 3) Ediacaran dolomite from subaerially weathered volcanics in Ukraine
78 (Liivamägi et al., 2021) (Table 1), and 4) U-Pb geochronology on *Microcodium* calcite from the Spanish Southern Pyrenees
79 that provided more constraints on fluvial mobility during the Paleocene–Eocene Thermal Maximum event (Prieur et al., 2024).
80 LA-ICP-MS U-Pb dating requires chemically homogenous and large enough zones (typically, between 50 and 200 μm wide
81 circles or squares) to obtain sufficient U and radiogenic Pb signals to produce meaningful age results (Roberts and Holdsworth,
82 2022). Additionally, high U and low common Pb concentrations are required to produce precise U-Pb dates, but carbonates
83 typically incorporate low U abundances (unless the precipitation takes place in reducing environments, e.g. Fournier et al.,
84 2004; Drake et al., 2018; Aguirre Palafox et al., 2024) and significant common Pb (Roberts et al., 2020). Carbonates in general
85 and pedogenic carbonates in particular, are also often heterogenous at the hundreds of micrometre scale or below (Zamanian
86 et al., 2016; Roberts and Holdsworth, 2022; Aguirre Palafox et al., 2024), partially explaining the paucity of reliable dating
87 results from pedogenic carbonates. More widespread absolute dating of pedogenic carbonates may provide valuable
88 chronostratigraphic constraints in continental successions, particularly those where volcanic horizons or index fossils are
89 absent. Aguirre Palafox et al. (2024) recently provided guidelines and strategies to improve the sampling and interpretation of
90 pedogenic carbonates, and addressed the influence of redox conditions on U concentrations and potential internal zonation.

Table 1: Summary of published U-Pb ages of terrestrial pedogenic carbonates (modified and updated after Rasbury and Cole, 2009).

Age Ma	$\pm 2\sigma$	MSWD	Max. U ppm	Technique	Material dated			Soil protolith	Reference
					Country	Rock	Mineral		
39.5	1.4	0.89	3.25	LA-SF-ICP-MS (spots)	USA	Pedogenic nodule	Cal	clastics & volcanics - continental	Methner <i>et al.</i> , 2016
40.1	0.8	1.15	3.44	LA-SF-ICP-MS (spots)	USA	Pedogenic nodule	Cal	clastics & volcanics - continental	Methner <i>et al.</i> , 2016
52.9	15	4.1	?	LA-SF-ICP-MS (spots)	Spain	Microcodium	Cal	sandstones - fluviatile	Prieur <i>et al.</i> , 2024
72	11	0.011	?	LA-SF-ICP-MS (spots)	Spain	Microcodium	Cal	sandstones - fluviatile	Prieur <i>et al.</i> , 2024
80.9	11	30	0.6	ID-TIMS	USA	Rhizolith	Cal, blocky	clastics - fluviatile	Wang <i>et al.</i> , 1998
211.9	2.1	2.67	2.7	ID-TIMS	USA	Calcrete	Cal, micritic	clastics - fluviatile	Wang <i>et al.</i> , 1998
212.4	3.4	3.4	2.5	ID-TIMS	USA	Calcrete	Cal, micritic	clastics - fluviatile	Wang <i>et al.</i> , 1998
228.4	5	1.7	7	LA-SF-ICP-MS (spots)	Argentina	Pedogenic nodule	Cal	clastics & volcanics - fluviatile	Aguirre Palafox <i>et al.</i> , 2024
230.5	2.2	1.1	40	LA-SF-ICP-MS (spots)	Argentina	Pedogenic nodule	Cal	clastics & volcanics - fluviatile	Aguirre Palafox <i>et al.</i> , 2024
233.6	3.9	0.89	120	LA-SF-ICP-MS (spots)	Argentina	Pedogenic nodule	Cal	clastics & volcanics - fluviatile	Aguirre Palafox <i>et al.</i> , 2024
254	29	504	29	ID-TIMS	USA	Dolocrete	Dol	carbonates - marine	Luczaj and Goldstein, 2000
275	6	?	?	ID-TIMS	USA	Paleosol	Cal	carbonates - lacustrine?	Becker <i>et al.</i> , 2001
282	28	417	32.5	ID-TIMS	USA	Dolocrete	Dol	carbonates - marine	Hoff <i>et al.</i> , 1995
294	6	?	?	ID-TIMS	USA	Paleosol	Cal	carbonates - lacustrine?	Becker <i>et al.</i> , 2001
294.9	8.6	2.2	~27	LA-Q-ICP-MS (map)	USA	Calcrete	Cal, sparry	carbonates - marine	Rasbury <i>et al.</i> , 2023
298.1	1.4	0.9	8.6	ID-TIMS	USA	Calcrete	Cal, sparry	carbonates - marine	Rasbury <i>et al.</i> , 1997, 1998, 2000, 2009
306	2.6	0.6	-	ID-TIMS	USA	Calcrete	Cal, sparry	carbonates - marine	Rasbury <i>et al.</i> , 1998
512	10	314	1.24	ID-TIMS	USA	Dolocrete	Dol	carbonates - marine	Winter and Johnson, 1995
548	19	1.3	0.57	LA-SF-ICP-MS (spots)	Ukraine	Weathered volcanics	Dol, blocky	volcanics - basalts, tuffs	Liivamägi <i>et al.</i> , 2018

Abbreviations: Cal = Calcite, Dol = Dolomite, ID-TIMS = Isotope Dilution Thermal Ionization Mass Spectrometer, LA-(SF/Q)ICP-MS = Laser Ablation (Sector Field/Quadrupole) Inductively Coupled Mass Spectrometry

A recent and innovative LA-ICP-MS U-Pb carbonate dating protocol, based on the selection and pooling of pixels from 2D elemental and isotopic ratio maps (Drost *et al.*, 2018; Roberts *et al.*, 2020; Chew *et al.*, 2021) is now commonly employed as a U-Pb dating strategy (e.g. Monchal *et al.*, 2023; Rasbury *et al.*, 2023; Subarkah *et al.*, 2024). This in-situ technique allows for the selection of chemically homogenous zones within a chemically heterogenous ablated 2D map area, reducing the risk of incorporating U-Pb data from non-carbonate inclusions or different generations of carbonates (Drost *et al.*, 2018). In addition, this method optimises the spread of data points in Tera-Wasserburg (TW) space increasing the precision of the results (Drost *et al.*, 2018). Therefore, this mapping-based technique is well suited to U-Pb dating and elemental characterisation of paleosol calcite, and can help alleviate some of the issues caused by microheterogeneity in pedogenic carbonates. A late Paleozoic paleosol calcite, already dated by ID-TIMS (298.1 \pm 1.4 Ma; Rasbury *et al.*, 1998) has been successfully dated using this approach (294.9 \pm 8.6 Ma; Rasbury *et al.*, 2023).

Continental sedimentary successions are often barren or poor in index fossils, which makes dating and intra-basin correlation difficult. Mammal remains have been used to create terrestrial biostratigraphic scales, such as the Neogene mammal (MN) scale in Western Europe (Mein, 1975; Agustí *et al.*, 2001). The European MN scale is similar to the North American Land Mammal Ages (NALMAs) and South American Land Mammal Ages (SALMAs) scales (see the review of Hilgen *et al.*, 2012). However, mammal fossils are not ubiquitous in the sedimentary record, thus the MN and other mammal scales cannot always be employed. When compared to marine biostratigraphic records (which have index fossils such as planktonic foraminifera, ammonites, graptolites, etc.), they also exhibit diachronicity and a poorer temporal resolution. The poor temporal resolution, particularly in the early stages of the MN scale (see Discussion) is well illustrated by the MN3 biozone, which has a duration of between 2.8 and 5.4 Myr, depending on the absolute age chosen for the top and bottom boundaries (Mein, 1999; Steininger, 1999; Aguilar *et al.* 2003; Raffi *et al.*, 2020). For comparison, the Paleogene calcareous nannofossil scale biozones all have a duration lower than 2 Myr, with most lower than 1 Myr (Agnini *et al.*, 2014). The LA-ICP-MS calcite U-Pb geochronology

114 approach adopted in this study has the potential to constrain the age of continental sedimentary horizons where pedogenic
115 nodules are present. This approach may improve inter-basin correlations, temporal resolution of the MN scale, as well as
116 potentially highlighting regional diachronism if more extensive sampling campaigns were conducted. In this study, we apply
117 the LA-ICP-MS U-Pb mapping technique along with spot analysis to obtain absolute ages from pedogenic calcite nodules
118 from a terrestrial Miocene succession in the Paris Basin, France, whose age is hitherto poorly constrained in terms of absolute
119 dating.

120 **2 Geological setting**

121 **2.1 Regional geology**

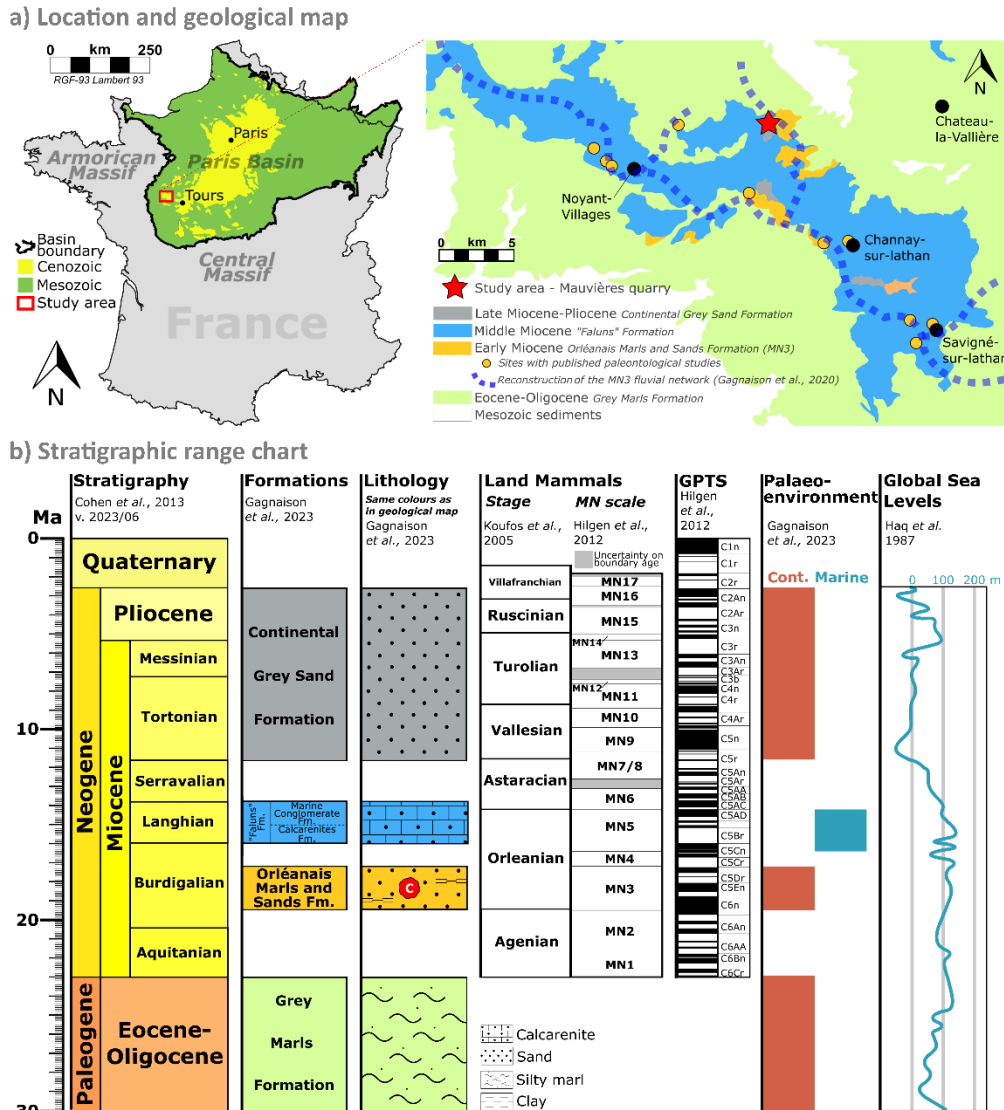
122 The Mauvières paleontological site is located in the SW of the Paris Basin (France), a Mesozoic-Cenozoic intracontinental sag
123 basin (Guillocheau et al., 2000). The site is on the northeast margin of the Neogene outcrops, which comprise continental and
124 marine sedimentary rocks unconformably deposited on Paleogene continental sedimentary rocks (Figure 1a). Regionally, the
125 Cenozoic sedimentary sequence reflects a dominantly continental paleoenvironment with occasional marine transgressions
126 during the Miocene (Figure 1b, Gagnaison, 2020).

127 **2.2 Paleoenvironment and origin of the calcite nodules**

128 The pedogenic nodules were sampled from the Early Miocene (early to middle Burdigalian) Orléanais Marls and Sands
129 Formation (Figure 1b), a few meters-thick succession of coarse and fine-grained clastic sediments (Figure 2). This Formation
130 rests unconformably over a Paleogene lacustrine silty marl (the Eocene-Oligocene Grey Marls Formation) and is overlain by
131 Middle Miocene marine shelly carbonate sands, known locally as “*faluns*” (Gagnaison et al., 2023) (Figure 1b and Figure 2).
132 The Early Miocene continental sequence at Mauvières consists of a series of eight clastic beds (numbered s1 to s8; Gagnaison
133 et al., 2023; Figure 2a). The pedogenic nodules were found in the basal bed s1, which overlies Eocene-Oligocene silty marls
134 (Figure 2). The s1 bed is comprised of a very coarse light grey-orangey quarzitic sand with minor feldspar, in-situ terrestrial
135 vertebrate fossils, poorly preserved *Unio* shells (a freshwater mussel), and in-situ carbonate nodules and cylinders. The sand
136 also contains reworked material, including Cretaceous calcareous and siliceous pebbles, altered glauconite grains, and
137 Cretaceous and Oligocene / Early Miocene vertebrate fossils. The sand is loosely cemented with a clayey and calcareous matrix
138 (Gagnaison et al., 2023). Some rare *Unio* shells have been found with both valves still connected, indicating both a low-energy
139 environment and that they are in-situ (i.e. not reworked from older beds).

140 The occurrence of 1) hollow calcite cylinders and nodules interpreted as rhizocreations, 2) root tracks in the matrix, 3) iron
141 oxides that give the sand its orange colour, and 4) microvacuoles interpreted as products of subaerial microbial activity, suggest
142 the presence of a paleosol (Gagnaison et al., 2023). The nodule-bearing s1 bed is interpreted as a water-transported, low-energy
143 fluvial sequence with prograding sand bars, with phases of lacustrine floodings and development of paleosols. The sequence
144 was subsequently subaerially exposed and followed by the development of a vegetated soil (Gagnaison et al., 2023). The

145 pedogenic nodules are consequently interpreted as in-situ and not reworked from older horizons. Rasbury et al. (1997) have
 146 shown that the calcite spar typically forms rapidly following paleosol development, and therefore absolute dating of the
 147 nodules should provide robust age constraints on the minimum age of the s1 bed. Based on detailed petrography including CL
 148 imaging, Aguirre Palafox et al. (2024) provided more information on the environmental factors that influence the timing of
 149 nodule formation (e.g. redox conditions, burial, water table levels) that can in turn help refine the interpretation of
 150 geochronological results.



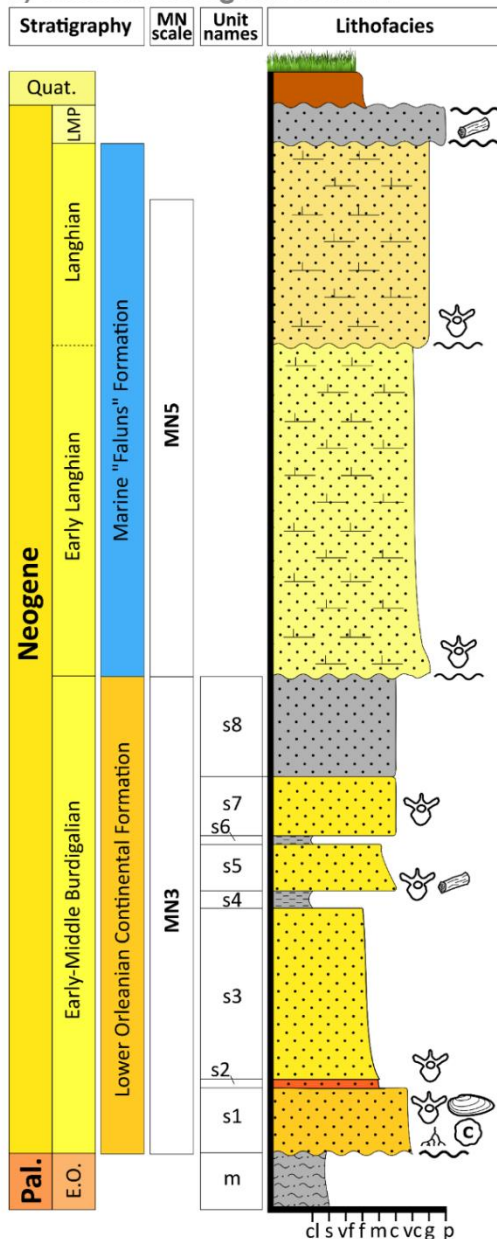
151 Figure 1: Geological context of the Mauvières section. a) Location of the Mauvières quarry and regional geology based on the
 152 BRGM 1/50,000 unified vector geological map of France (InfoTerre), modified after Gagnaison et al. (2020). b) Stratigraphy of the
 153 Mauvières section. The nodules (red symbol with a C) come from the Orléanais Marls and Sands Formation attributed to the MN3
 154 biozone (Gagnaison et al., 2023). V. 2023/06 : The 6th International Chronostratigraphic Chart of the International Commission of
 155 Stratigraphy (2023). GPTS : Geomagnetic Polarity Time Scale.

156 **2.3 Biostratigraphic age of the continental sands and nodule-bearing s1 bed**

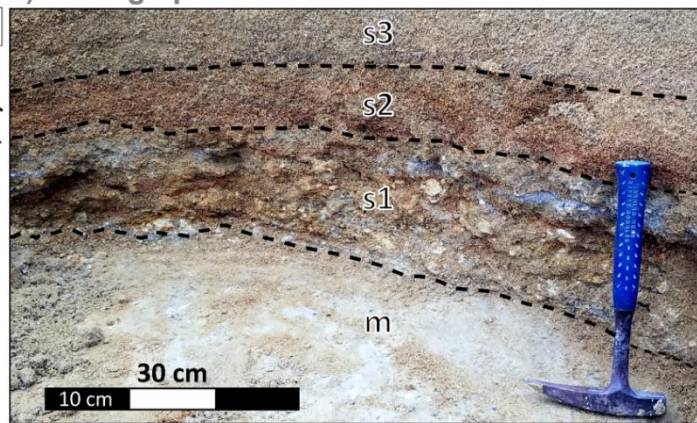
157 MN biozones were defined as a tool for inter-basin faunal comparisons (Mein, 1999). Limits of the zones are defined by 1)
158 steps in mammalian evolutionary lineages (local evolution), 2) First Appearance Datum and/or Last Appearance Datum of
159 species, 3) dispersal of taxa, and 4) faunal assemblages (Mein, 1999; Steininger, 1999). As discussed by Mein (1999), even
160 when relatively inaccurate, the MN-zones are still a useful tool for regional correlation. For example, where local mammalian
161 biozones are developed (e.g. the Mongolian Mammalian biostratigraphy proposed by Daxner-Höck et al., 2017), the MN
162 system can still be employed since Europe and Asia often share taxa (Wang et al. 2013). However, we should keep in mind
163 that correlation using the MN timescale is affected by ecological limits, latitudinal disparities, general diachronism in the
164 dispersion of taxa, the presence of immigrant taxa (Mein 1999; Steininger, 1999) and local differences in taxa (even between
165 neighbouring basins; Engesser and Mödden 1997).

166 Regionally, both the continental and marine Miocene sediments are known for their rich fauna of vertebrate fossils, including
167 mammal taxa (Ginsburg, 2001). At Mauvières, vertebrate remains have been found within four horizons within the Orléanais
168 Marls and Sands Formation (Figure 2a). The majority of fossils (>95%) are fresh and thus interpreted as syn-sedimentary and
169 not reworked from older beds. In total, 53 taxa have been identified, most of them present in the s1 bed, the richest of the four
170 fossiliferous horizons. The taxa are typical of the middle of the MN3 biozone (Gagnaison et al., 2023) (Figure 1b and Figure
171 2a).

172 a) Sedimentological column



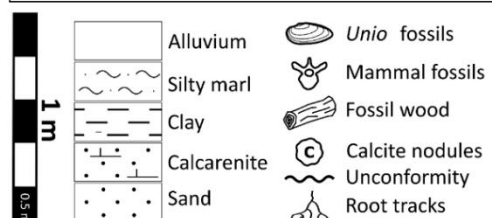
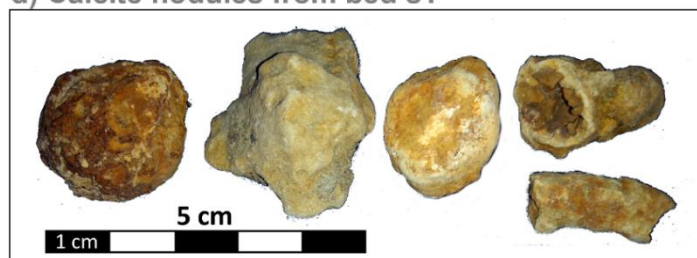
173 b) Photograph of the bottom section of the outcrop



174 c) Photograph of s1 bed nodules and clasts



175 d) Calcite nodules from bed s1



176 Figure 2: Geology of the Mauvières section. a) Sedimentological log and bed nomenclature (modified after Gagnaison et al., 2023).
177 The calcite nodules are found in the Early-Middle Burdigalian basal sand s1. b) Photograph of the basal section of the outcrop,
178 showing the basal Paleocene-Eocene silty marls unconformably overlain by an orange, very coarse fluvial sand with mammal
179 remains, freshwater mussel shells, root tracks and pedogenic calcite nodules. c) Granule and pebble fraction after sieving of the s1
180 sand. The fraction is dominated by pale-coloured calcite nodules. d) Photographs of representative calcite nodules from the s1 bed
181 showing both spherical and cylindrical irregularly-shaped nodules of varying colour.

179 **3 Materials and methods**

180 **3.1 Samples**

181 Between 2020 and 2022, a series of geological sampling campaigns were undertaken at the Mauvières site. The sample material
182 was sieved, washed, and dried. From the coarse separate (>2 mm), numerous nodules were collected and identified as vadose
183 carbonate nodules (Gagnaison et al., 2023). The nodules are spherical to oblong, with a yellow-orange colour and a coarse
184 aspect. Five of these nodules were selected for SEM elemental analysis and U-Pb dating (P00, P01, P02, P04, and P14), three
185 nodules for powder X-ray diffraction analysis (XRD), and one nodule was prepared as a thin section for detailed microscopic
186 analysis (MIOC4). For XRD analysis, each selected nodules were crushed in an agate mortar to create a fine powder. The five
187 other nodules selected for U-Pb dating were sawn in half to reveal an internal surface. One half of each nodule was mounted
188 in a 25 mm mould, mounted in epoxy resin, cured and polished, with the final polishing step employing 1 μ m diamond
189 suspension polishing fluid. The epoxy resin mounts were cleaned in an ultrasonic bath of deionized water for three minutes
190 and imaged by optical microscopy. LA-ICP-MS U-Pb dating was undertaken on sample P00 to see if high quality age data can
191 be obtained from the sample suite. Following LA-ICP-MS analysis of sample P00, it was repolished to remove the ablation
192 rasters, cleaned in an ultrasonic bath of deionized water and carbon coated for SEM analysis. The other four samples were first
193 carbon coated for SEM analysis, and later polished and then cleaned to remove the carbon before subsequent LA-ICP-MS
194 analysis.

195 **3.2 Optical microscopy**

196 The resin pucks were imaged under reflected light using a Nikon Eclipse LV100 at the iCRAG Lab@TCD, Trinity College
197 Dublin. Images were acquired at 5x magnification using a Nikon DS-Ri2 camera. Each tiled image is comprised of multiple
198 frames stitched together by the Nikon NIS-Elements software. Each frame was taken with a square field of view of c. 2.8 mm
199 in width and with an overlap of 10%. Transmitted and plane-polarised light images were also acquired for thin section MIOC4.

200 **3.3 XRD**

201 The powders were analysed using a Siemens/Bruker D5000 power X-ray diffractometer (Cu K α radiation, 0.01 $^{\circ}$ step $^{-1}$ from
202 5 to 60 $^{\circ}$ 2 θ at 1 $^{\circ}$ min $^{-1}$, 4.5 hours per sample). Mineral identification was undertaken with DIFFRAC.EVA (Bruker) using
203 the Powder Data File (PDF-4, The International Centre for Diffraction Data) (Gates-Rector and Blanton, 2019). XRD results
204 and its interpretation are available in the Supplementary Materials.

205 **3.4 SEM**

206 The SEM analyses were carried out at the iCRAG Lab@TCD (Trinity College Dublin, Ireland) on a Tescan TIGER MIRA3
207 FEG-SEM equipped with a backscatter electron detector (BSE), two Oxford Instruments Ultim Max 170 mm 2 SSD EDX
208 detectors and an X4 pulse processor. Scanning electron (SE) and BSE imaging and energy-dispersive X-ray spectroscopy

209 (EDS) analyses were acquired using an accelerating voltage of 20 kV and a working distance of 15 mm above the carbon-
210 coated pucks. The images and maps were processed using the AZtec version 6.1 X-ray microanalysis software suite (Oxford
211 Instruments).

212 **3.5 Cathodoluminescence**

213 Polished and uncovered carbon-coated thin sections for each sample were imaged using optical CL microscopy. CL images
214 were acquired at University College Dublin (UCD) using an HC5-LM hot-cathode CL microscope from Lumic Special
215 Microscopes, operated at 12.2 kV with a current density of 0.24 mA.mm⁻². No staining solution was applied prior to the
216 imaging.

217 **3.6 LA-Q-ICP-MS**

218 Laser ablation Q(quadrupole)-ICP-MS U-Pb dating was performed at the iCRAG Lab@TCD, Trinity College Dublin,
219 employing an Iridia 193 nm ArF excimer LA system (Teledyne Photon Machines, Bozeman, MT, USA) coupled to an Agilent
220 7900 Q-ICP-MS via 1.016 mm ID PEEK tubing and a medium pulse interface. One sample (P00) was dated using a mapping
221 approach and follows the U-Pb imaging technique described in Drost et al. (2018), while the remaining samples (P00-repeat,
222 P01, P02, P04, P14) were analysed by static spot analysis. For the latter, signal smoothing was achieved by inserting a mixing
223 chamber (Glass Expansion) between medium pulse interface and torch. Details on the specific analytical protocol and operating
224 conditions are given in the supplementary material (Supplementary Table 1-6 and Supplementary Document 1). This includes
225 the selection criteria, regions of interest, map dimensions and time-equivalents for all selected pixels and pixel groups ('pseudo-
226 analyses') for the sample analysed with the mapping approach, and the laser pit locations of the samples analysed by spot
227 ablation. Supplementary Tables are available on the Zenodo repository system (Monchal et al., 2024) while Supplementary
228 Document and Figure are available with the online version of this manuscript.

229 Samples were first screened for suitability using line scans. Samples and sample area yielding high initial Pb concentrations
230 and low μ throughout were omitted from further analysis. Similarly, samples areas with $U \leq 10$ ppb were ignored as the young
231 sample age would result in very low concentrations of radiogenic Pb. Final locations for U-Pb analysis were selected according
232 to the results of the test line scans in combination with mineralogical and textural observations from optical microscopy and
233 from chemical information obtained by SEM-EDS mapping. In each dated nodule, we targeted calcite zones with minimal
234 incorporation of other phases. For the mapping experiment, this resulted in multiple groups of raster lines spread out across
235 the nodule surface. Final ROIs for data extraction were chosen to represent zones that may be interpreted as cogenetic and thus
236 a single age population constraining cementation. However, samples P01, P02, P04, and P14 did not feature large enough
237 coherent calcite areas with Pb/U ratios favourable for efficient and reproducible use of the mapping protocol. Spot analysis
238 was subsequently performed on those samples, using the chemical information from the SEM and LA-ICP-MS maps to help

239 site the spot analyses. Additionally, the U-Pb mapping data from sample P00 was also augmented by a static spot ablation
240 experiment.

241 The mapping session employed a laser spot size of 80 μm square, a repetition rate of 50 Hz and a fluence of 2.5 J/cm^2 while
242 moving the sample along successive linear rasters with 30 $\mu\text{m}/\text{s}$ under the static laser beam. Samples were bracketed by NIST
243 SRM 614 glass as the primary standard, WC-1 calcite for matrix-matching the $^{206}\text{Pb}/^{238}\text{U}$ ratio (Roberts et al., 2017) and Duff
244 Brown Tank limestone as quality control material (Hill et al., 2017). The total analysis time for sample P00 was c. 34 minutes.
245 Spot analysis employed 85 μm diameter spots, a repetition rate of 12 Hz, 480 shots (40s) and a fluence of 2.2 J/cm^2 . Again,
246 NIST SRM 614 was used as the primary standard, but Duff Brown Tank limestone was used for matrix-matching of the
247 $^{206}\text{Pb}/^{238}\text{U}$ ratio as it is closer in U concentration and age to the samples than WC-1. Gas settings (optimised daily), analyte
248 menus and integration times for all analytical sessions are reported in Supplementary Doc 1 along with the data processing
249 protocols used.

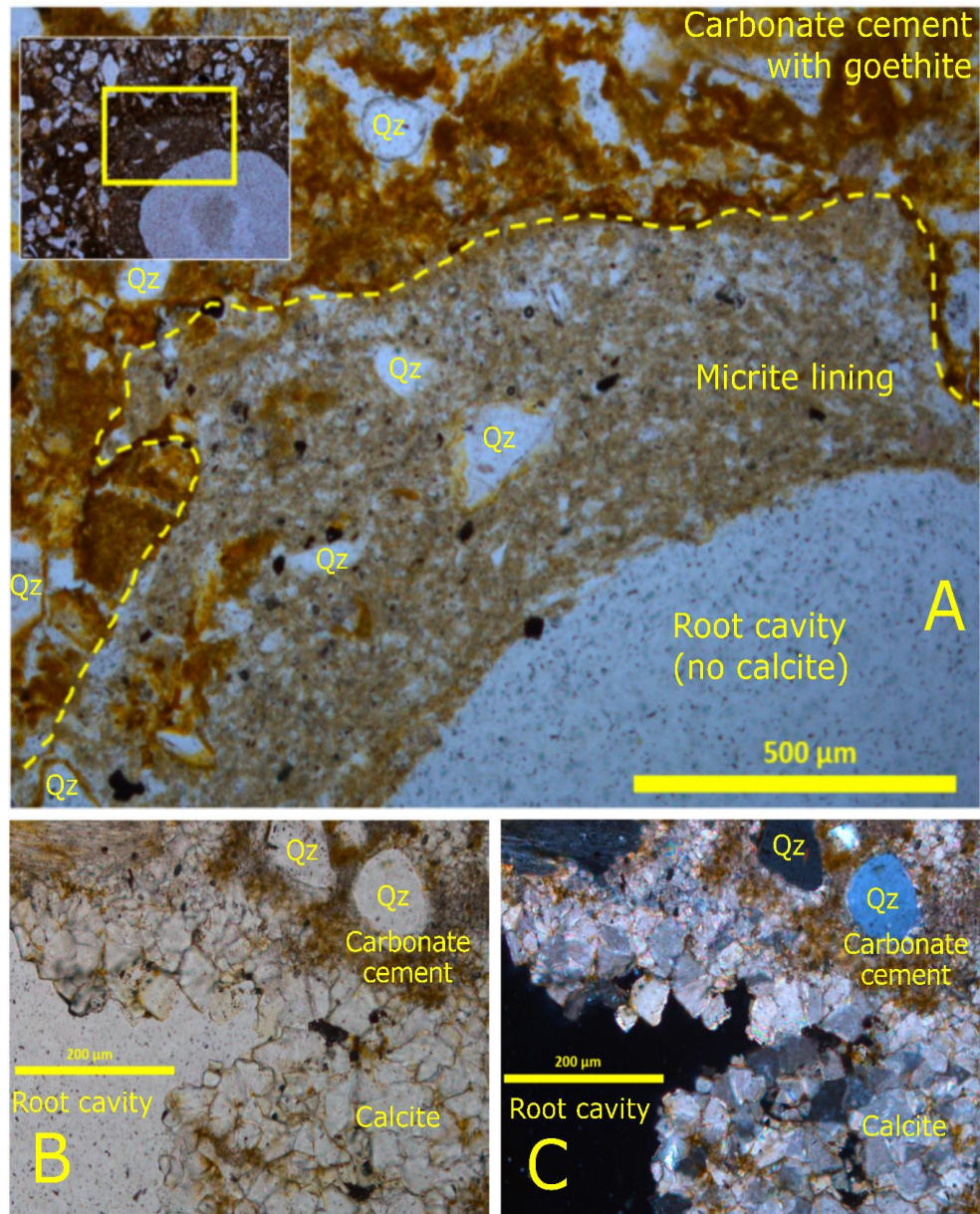
250 Uncertainties on dates in the text and figures are quoted at the 2σ or 95% confidence level, respectively. The geochronological
251 results are presented with two uncertainties; the first is an estimate of the session uncertainties, while the second is propagated
252 with full systematic uncertainties (e.g., the uncertainty on the reference age of WC-1 (maps) or DBT (spots) respectively, the
253 decay constant uncertainties, and the 2% long-term reproducibility of secondary age reference materials in the laboratory; see
254 Supplementary Document 1).

255 4 Results

256 4.1 Petrographic observations

257 The samples are composed of transparent, mostly rounded quartz grains with some more angular crystals, set in a pale orange-
258 yellow cement with vein-like cavities, partially filled with carbonate crystals (Figure 3). The majority of the samples exhibit a
259 main cavity that in some cases branches out *via* micro-cracks, typical of alpha type paleosoil (Wright, 1990). We can
260 distinguish two stages of formation. The first stage involves the formation of sedimentary concretions around roots. The
261 concretions are rich in quartz and cemented by clear carbonate as observed under the optical transmitted light microscope
262 (Figure 3). After decomposition of the roots, sparry carbonate crystals precipitated predominantly into free space producing a
263 brown layer on the edge of the cavity and filling the micro-cracks. The host-rock is composed of touching or floating
264 terrigenous clastic elements such as quartz in a clotted carbonated matrix with authigenic goethite. The host-rock is also cross-
265 cut by rhizolith root tubules, traces of which are still visible (Figure 3A). These relics of paleo-roots are expressed by the stack
266 of several layers of dark microbial micrite linings (Figure 3A) and some holocrystalline microsparite. The presence of
267 holocrystals is dependent on the degree of microbial activity and the root structure (i.e. main axis *vs* lateral roots). These early
268 pedogenic carbonate crystals (e.g. the calcite crystals in Figure 3B-C) are classically found in many paleosols (e.g. Wright,
269 1987; Esteban and Klappa, 1983; Bain and Foos, 1993; Alonso-Zarza, 2003).

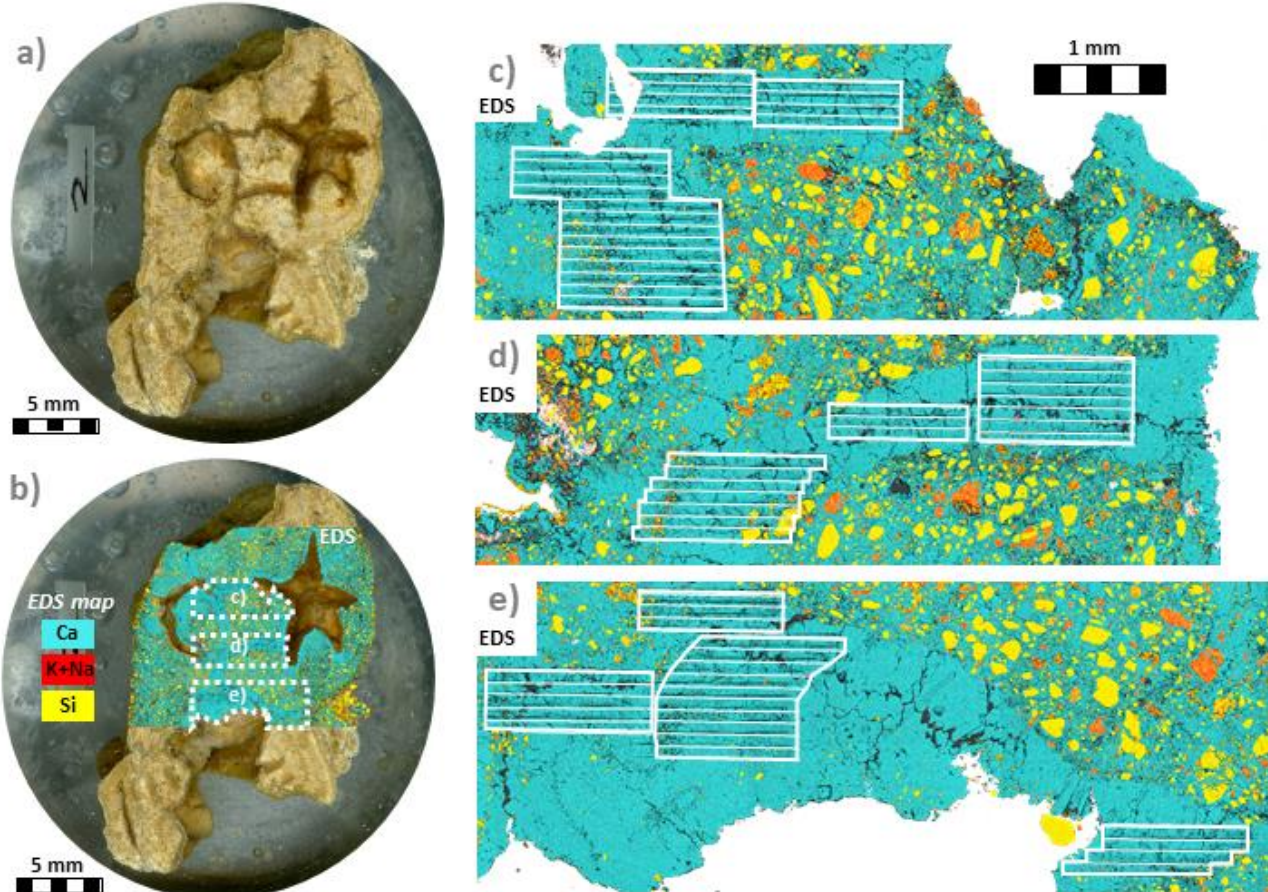
270 Sample MIOC4 is a representative nodule from the s1 bed that exhibits evidence of primarily calcified root traces (Figure 3; 271 see also Gagnaison et al., 2023). No evidence of later crystallisation nor recrystallisation was detected, with the calcite spar 272 homogeneous and unzoned (Figure 3B-C). Moreover, micro-cracks and alveolar structures are commonly found without 273 calcite crystallisation (Figure 3A), especially where the primary root was located. When calcite crystals are present, they are 274 typically associated with lateral roots.



275 Figure 3: Optical microscope photography of sample MIOC4. A) Primary root structure with a dark microbial micrite lining – 276
277 dashed yellow line highlights the boundary of the external part of the microbial micrite lining. An alveolar structure can be seen on 278 the zoomed out insert at the top of the microphotograph (PPL). B) Sparry calcite crystals; a lateral root perforation is on the lower left side of the microphotograph (PPL) and C) (XPL). Q = Quartz.

279 **4.2 SEM-EDS elemental mapping**

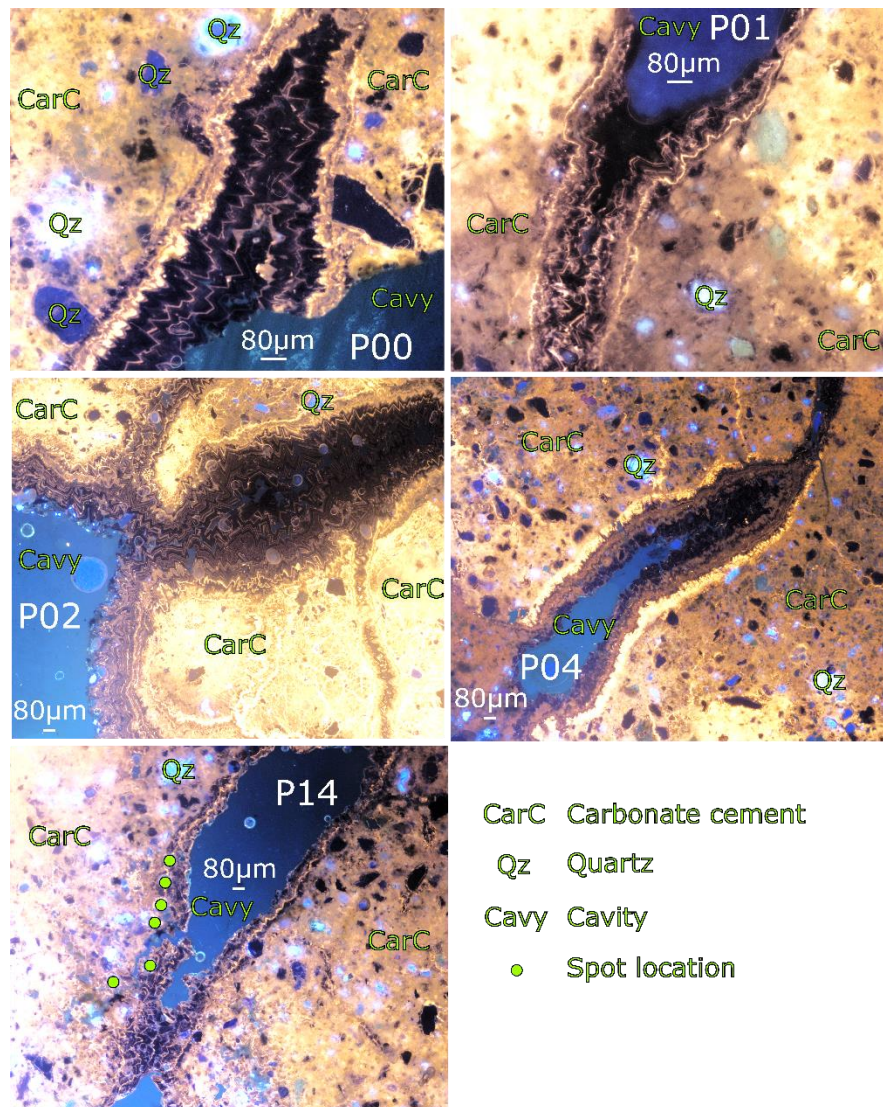
280 The SEM-EDS maps of the five dated nodules reveal that the nodules are composed of poorly sorted angular Si-rich minerals
 281 cemented by a Ca-rich phase (Figure 4). The two phases are interpreted respectively as quartz and calcite based on optical
 282 microscopy and the PXRD results. The cemented sand also contains grains rich in Si and K, Na interpreted as feldspar and in
 283 agreement with the results of PXRD. Large cavities, mostly branching or rounded are present in all the nodules. These cavities
 284 are lined by a pure Ca-rich phase interpreted as calcite that precipitated into the free cavity space. In some locations, quartz-
 285 free calcite crystals have filled the cavities entirely. These zones of pure calcite were subsequently targeted for LA-ICP-MS
 286 U-Pb dating.



287 **Figure 4: Photographic montage of nodule P00 in a polished resin puck. a) optical microscopy image b) the same image overlain by**
 288 **a partial EDS map of the nodule showing Ca (a proxy for calcite, blue), Si (a proxy for quartz, yellow), and K+Na (a proxy for**
 289 **feldspar, red). The location of the EDS maps in c), d), and e) are represented by the dashed white polygons. c), d), and e) EDS maps**
 290 **showing the LA-ICP-MS ablation zones and line scans for the P00 nodule. Pure calcite veins were targeted, avoiding the zones of**
 291 **calcite-cemented quartz-rich sand. See Supplementary Materials for pictures and EDS map of the other samples (Supplementary**
 292 **Figure 1).**

293 **4.3 Cathodoluminescence imaging**

294 The calcite-cemented sands in the concretions show a complex pattern of dull brown and orange to bright yellow luminescent
295 calcite cementing quartz and minor feldspars which are highly (and variably) luminescent. Sparry carbonate crystals infilling
296 cavities and fractures show strong oscillatory CL zoning at the $<10\text{ }\mu\text{m}$ scale (Figure 5). The calcite growth in the fractures
297 oscillates between non-luminescent, dull brown to orange luminescence, and bright yellow and orange luminescence. Growth
298 morphologies from CL are euhedral to occasionally subhedral blocky with no recrystallisation of the oscillatory zoning
299 observed.

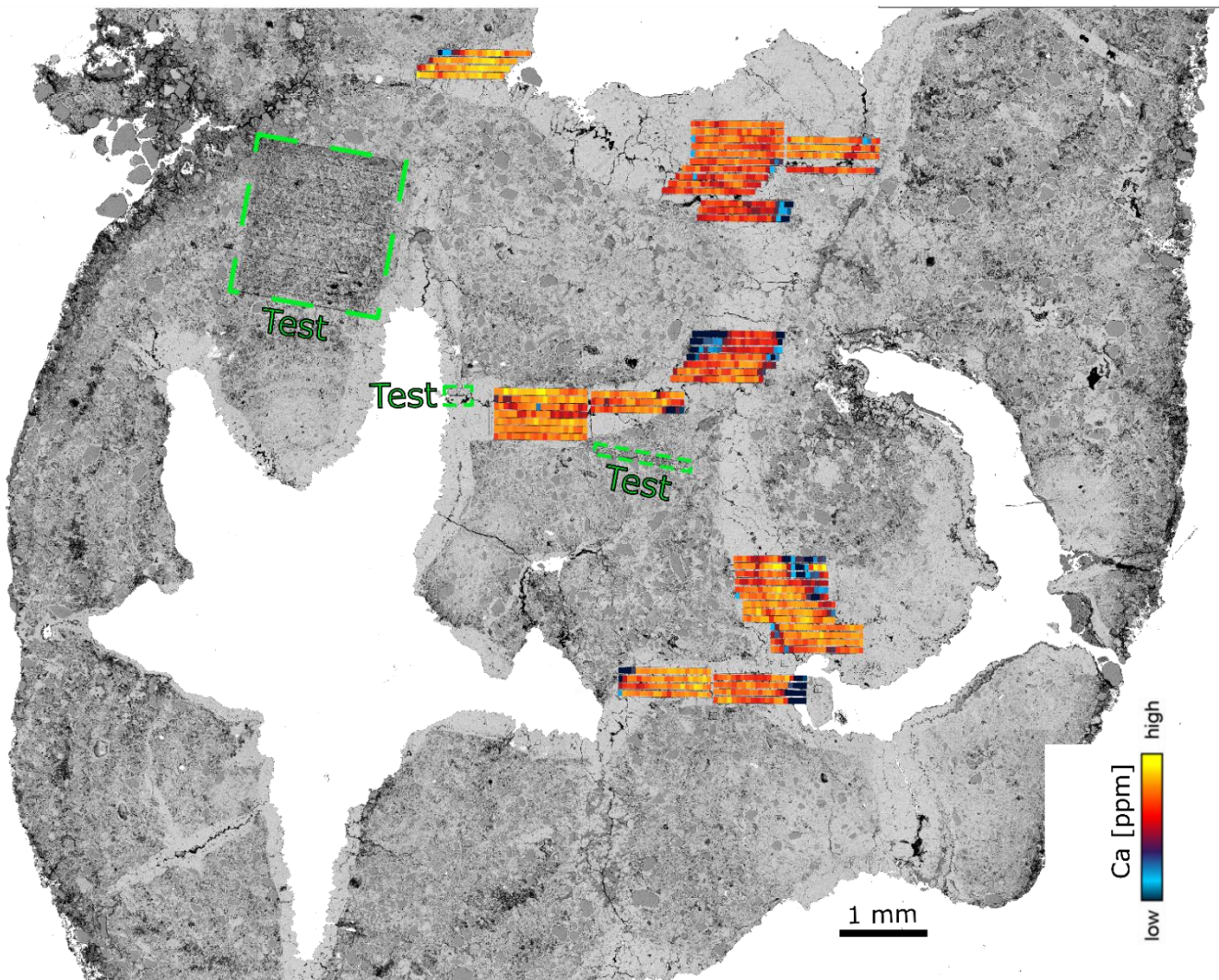


300
301 **Figure 5:** Cathodoluminescence images from the samples at 5x (P02/P04/P14) or 10x (P00/P01) magnification illustrating the
302 oscillation between non-luminescent dull brown and orange luminescent zonation in the calcite crystals. Spot locations are shown
on the P14 photo showing that the outer margins of the calcite zones were ablated.

303 **4.4 LA-ICP-MS U-Pb dating**

304 Calcite crystals that have precipitated freely inside the cavities were targeted for geochronology analysis (Figure 6) as they are
305 believed to have precipitated rapidly after the formation of the paleosol (see section 2.2 and Rasbury et al., 1997). The mapped
306 areas in P00 targeted zones of pure calcite based on the SEM-EDS mapping. A Ca filter (e.g. retaining pixels with Ca > 350
307 000 ppm) was applied on the P00 map to exclude any inclusions, cracks, epoxy resin or the host sedimentary rock and this
308 filter removed c. 7% of the pixels from the maps. The average U content is ~ 10 µg/g (ranging from 9 to 13 µg/g), while the
309 average Th content is ~ 0.7 µg/g (ranging from <0.1 to 2.5 µg/g; see Supplementary Table 1) resulting in Th/U ratios of <0.01
310 to <0.2. Significant initial Pb concentrations (~0.44 to 33 µg/g) and the long half-life of Th in combination with the young age
311 of the samples render the radiogenic ingrowth of radiogenic ^{208}Pb negligible ($^{208}\text{Pb}_{\text{common}}/^{208}\text{Pb}_{\text{radiogenic}} \sim 2800$ to 12000).
312 Therefore, we used the empirical cumulative distribution function of the $^{238}\text{U}/^{208}\text{Pb}$ channel for pooling of the filtered pixel
313 data into pseudo-analyses. The $^{238}\text{U}/^{208}\text{Pb}$ channel is a good estimate of the μ ratio between parent U (^{238}U) vs initial Pb (^{204}Pb)
314 as the total ^{208}Pb concentration is a robust proxy for the initial $\text{Pb}_{\text{common}}$ component.

315 The spot U-Pb data were corrected post-analysis for any ablation that went through the calcite. This correction employ the
316 visual inspection of peaks for a significant change in Ca, Pb, Th or U composition that indicate a change in the phase ablated.
317 The U-Pb spot analyses on samples P01, P02, P04 and P14 yielded dates of $18.8 \pm 2.7/2.7$ Ma, $19.11 \pm 0.84/0.94$ Ma, 19.0
318 $\pm 2.3/2.3$ Ma, $19.4 \pm 2.7/2.7$ Ma, respectively, while sample P00 yielded dates of $19.3 \pm 1.3/1.4$ Ma (mapping) and $19.7 \pm 1.5/1.6$
319 Ma (spots) (Figure 7). A radial plot and weighted average age were calculated using the five dates from spot analysis and their
320 respective internal uncertainties (session estimates) featuring a Mean Square Weighted Deviation (MSWD) and chi-square
321 ($p[\chi^2]$) test representing how good the results are fitting to the statistic value. The full systematic uncertainties (section 3.6)
322 were propagated onto the resultant age (radial plot or weighed average) calculation. The radial plot in Figure 8 shows a single
323 age group at $19.22 \pm 0.66/0.79$ Ma ($p[\chi^2] = 0.96$) and a weighted average age was calculated at $19.21 \pm 0.64/0.77$ Ma
324 (MSWD=0.16; $p[\chi^2] = 0.96$; see Figure 8). All U-Pb spot data were also plotted in the same Terra-Wasserburg space with
325 their individual propagated uncertainties providing a result of $19.1 \pm 0.56/0.71$ Ma. The radial plot single group age of
326 $19.22 \pm 0.66/0.79$ Ma is the preferred age adopted in this study as discussed in section 5.2.



327 **Figure 6: BSE image of P00 overlaid by the LA-ICP-MS line rasters used to extract the age. This figure shows that the pristine**
 328 **calcite was targeted by our analysis.**

327
328

329 **5 Discussion**

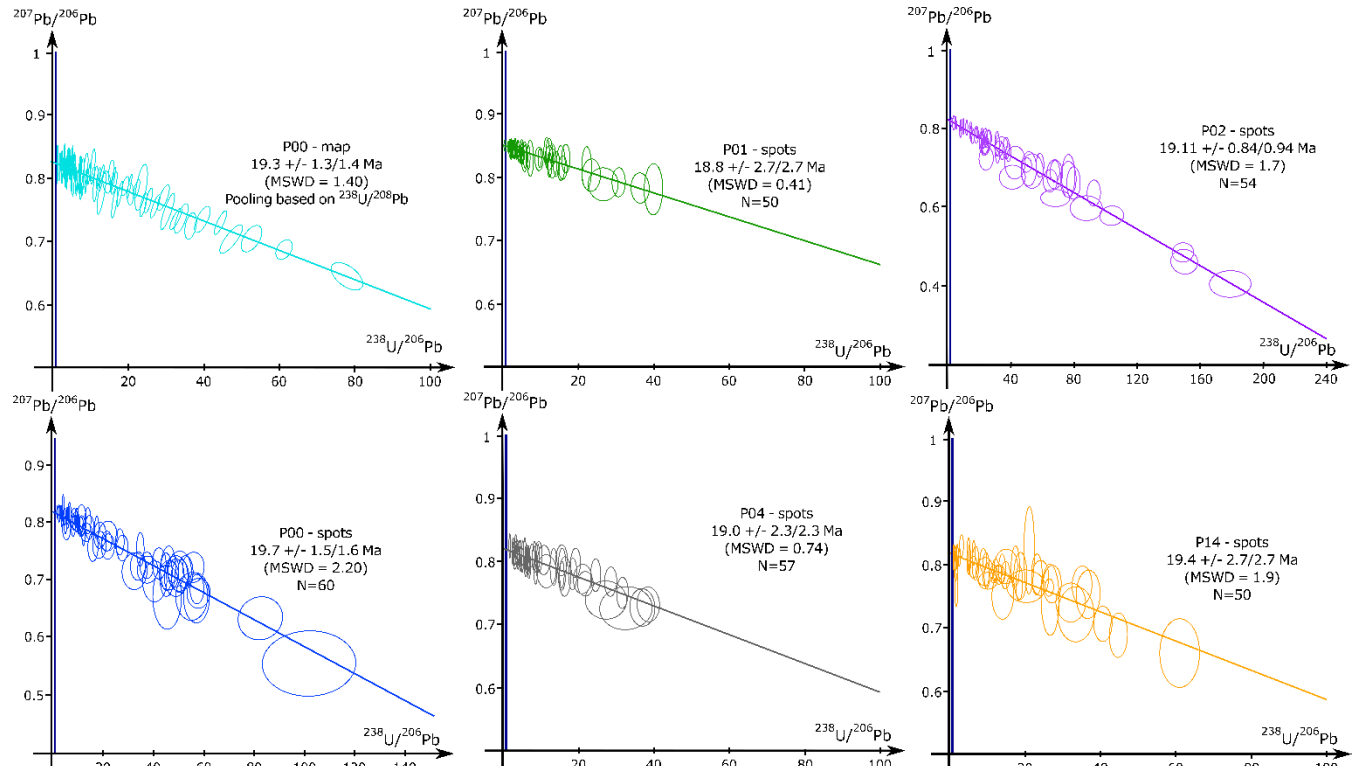
330 **5.1 Accuracy and precision of the U-Pb ages**

331 The imaging techniques (optical microscopy, SEM-EDS and LA-ICP-MS mapping) have differentiated zones of pristine
 332 calcite and the pervasive cementation of the nodules. Optical microscopy evidence favours the hypothesis of preservation of
 333 pristine calcite in our samples (see Results section 4.1). In addition, prior to their extraction from the s1 bed, all the pedogenic
 334 nodules (along with clasts and fossil material) were coated with an impermeable clay layer, which likely hindered subsequent
 335 passage of fluid into the nodules. The clay coating is interpreted as syn-sedimentary (see figures 2b-d and Gagnaison et al.,

336 2023). This sealed system is another argument in favour for the preservation of pristine calcite (Perry and Taylor, 2006) in the
337 nodule interiors (See Figures 4 and 5). The nodule morphology is preserved (not rolled or broken) and does not feature any
338 sign of compaction nor internal collapse which supports the hypothesis of non-reworked nodules. Tubular nodules have also
339 been found perpendicular to the stratigraphy, thus clearly marking the former position of the root. The Eocene-Oligocene marls
340 (m on Figure 2) below the s1 bed do not contain nodules, further supporting the hypothesis that the nodules found in the s1
341 bed are in-situ.

342 The growth morphologies from optical and CL microscopy indicate gradual growth competition took place, indicative of a
343 crystallisation in a cavity that remained open (e.g. Wendler et al., 2016; Prajapati et al., 2018). The oscillatory zoning with
344 multiple bright concentric subzones observed under CL (Fe is the main CL quencher and Mn the main activator) can be
345 explained by small yet rapid variations in Eh/pH conditions accompanied by changes in oxidation state (e.g., Pagel et al.,
346 2000). With increasing oxidation, Fe^{2+} and Mn^{2+} sensitized by Pb^{2+} and/or Ce^{3+} (Pagel et al., 2000) are replaced by Fe^{3+} and
347 Mn^{3+} or Mn^{4+} ions (e.g. Richter et al., 2003; Boggs and Krinsley, 2006). A plot of $\log [\text{Fe}]/\log [\text{Mn}]$ ppm can predict if calcite
348 will be bright, dull or non-luminescent in CL (Machel and Burton, 1991; Boggs and Krinsley, 2006) (see Supplementary
349 Material). The specific CL patterns are consistent with redox fluctuations caused by water table fluctuations in a vadose or in
350 a fluid-saturated environment (Mason, 1987; Barnaby and Rimstidt, 1989), which is also in agreement with the previous paleo-
351 environment reconstitutions for the s1 bed (Gagnaison et al., 2023). Given the above observations and since the oscillatory
352 zoning is continuous, we interpret a single continuous event of calcite formation to have occurred inside the nodules. The
353 differing thickness of the CL bands appears related to the size of each cavity in the nodules, with P00/P01/P02 having the
354 largest cavities and bands while nodules P04 and P14 have thinner bands.

355



356
357 **Figure 7: Tera-Wasserburg concordia diagrams and lower intercept ages of all samples. For the map analysis of P00, the pooling**
358 **was based on the ECDF $^{238}\text{U}/^{208}\text{Pb}$. For the spot analysis, the number of spots is indicated by N.**

358 The LA-ICP-MS mapping technique adopted herein is recognised for its potential (see Rasbury et al., 2023) in dating
359 pedogenic nodules by allowing the selection of only pristine calcite in the extraction and processing of the U-Pb data. However,
360 only one sample had large enough coherent zones of pristine calcite with Pb/U ratios suitable for U-Pb dating and a spot
361 analysis strategy was used to date the remaining four samples. All six results yield ages with a precision of 5 to 14%, which is
362 considered precise for LA-ICP-MS carbonate U-Pb dating of such young samples (Roberts et al., 2020). The accuracy of our
363 data set can be assessed by the fact that the five samples provide the same age and initial $^{207}\text{Pb}/^{206}\text{Pb}$ within uncertainties, along
364 with the radial plot confirming that there is only one age group (Figure 8). The accuracy of the mapping experiment is also
365 demonstrated by the similar dates (within uncertainties) yielded using three different isochron approaches. The mapping
366 approach data for sample P00 (using $^{238}\text{U}/^{208}\text{Pb}$ as the pooling channel) yields $19.3 \pm 1.3/1.4$ Ma for the TW intercept age,
367 $19.6 \pm 1.7/1.8$ Ma for the $^{238}\text{U}/^{208}\text{Pb}_{\text{common}}$ isochron (e.g., Getty et al., 2001) and an 86TW age (Parrish et al., 2018) of
368 $19.4 \pm 1.6/1.7$ Ma (section 3.4 and Supplementary Table 1).

369

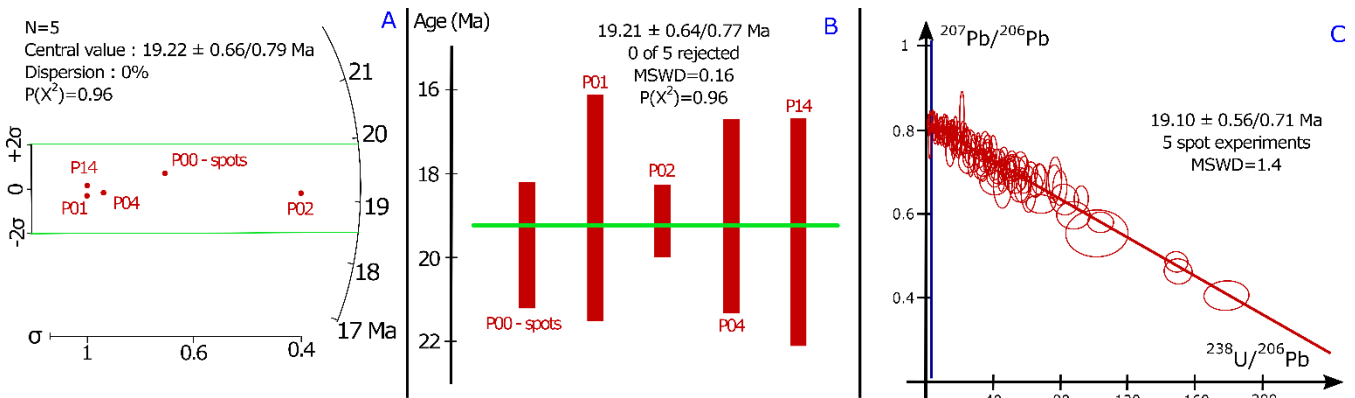


Figure 8: A) Radial plot and B) weighted average of the samples used in this study. Radial plot central value and the weighted average value are indicated with 2σ internal uncertainties (session estimates). The full systematic uncertainties (section 3.6) were propagated onto the resultant age calculations with the same method as for the individual sample ages. C) Tera-Wasserburg concordia diagram of all five spot ablation experiments. See text for the interpretation and discussion of the data.

5.2 Age of the nodules and paleosol

Our age data are compatible within uncertainty with the proposed biostratigraphic age of the continental biozone MN3, which is correlated with the Burdigalian marine stratigraphic age (20.44 - 15.98 Ma; Cohen et al., 2013 [updated 2023/09]) and the Orleanian continental stratigraphic age (19.5 - 14.2 Ma; Hilgen et al., 2012). Dating the pedogenic calcite should provide a minimum age for the paleosol formation (Rasbury et al., 1997). The nodules are found within the same sedimentary layer (section 2.2) and we can therefore reasonably assume that the crystallisation of the calcite inside each nodule arose from the same process(es). Even if these process(es) involve multiple phases of growth, we do not see any evidence of incremental growth of more than one generation of calcite from petrography, CL and SEM-EDS mapping. The U/Pb dates obtained on these five nodules are identical within age uncertainty of our method (Fig. 8) and do not exhibit evidence for more than one stage of calcite growth, diachronous growth across different nodules or a substantial time span between initiation and termination of calcite formation. We therefore assume that formation of the analysed nodules (which are identical within age uncertainty of our method) was effectively synchronous.

To determine the minimum age of nodule formation, there are several possible approaches: 1) the U/Pb date with the lowest uncertainty (P02: $19.11 \pm 0.84/0.94$ Ma), 2) the date derived from the combined TW regression of spot analyses from all five samples (Fig. 8C; $19.10 \pm 0.56/0.71$ Ma), 3) a weighted mean of the U/Pb dates from all analysed samples (Fig. 8B; $19.21 \pm 0.64/0.77$ Ma) or 4) the radial plot age (Fig. 8A; $19.22 \pm 0.66/0.79$ Ma). The former two methods may introduce some bias as they may overly rely on the data points with the highest $^{238}\text{U}/^{206}\text{Pb}$ ratios coming all from the same sample (P02), while the latter two methods put more emphasis on the similarity of the results associated with individual samples. The radial plot shows only one age group, and the central age from the radial plot and the weighted mean of the TW intercept ages are identical within age uncertainty. The weighted mean age calculation assumes the data follows a normal distribution, while the radial plot assumes that the log of the values follows a normal distribution curve (Vermeesch, 2018). Geochronological data are less

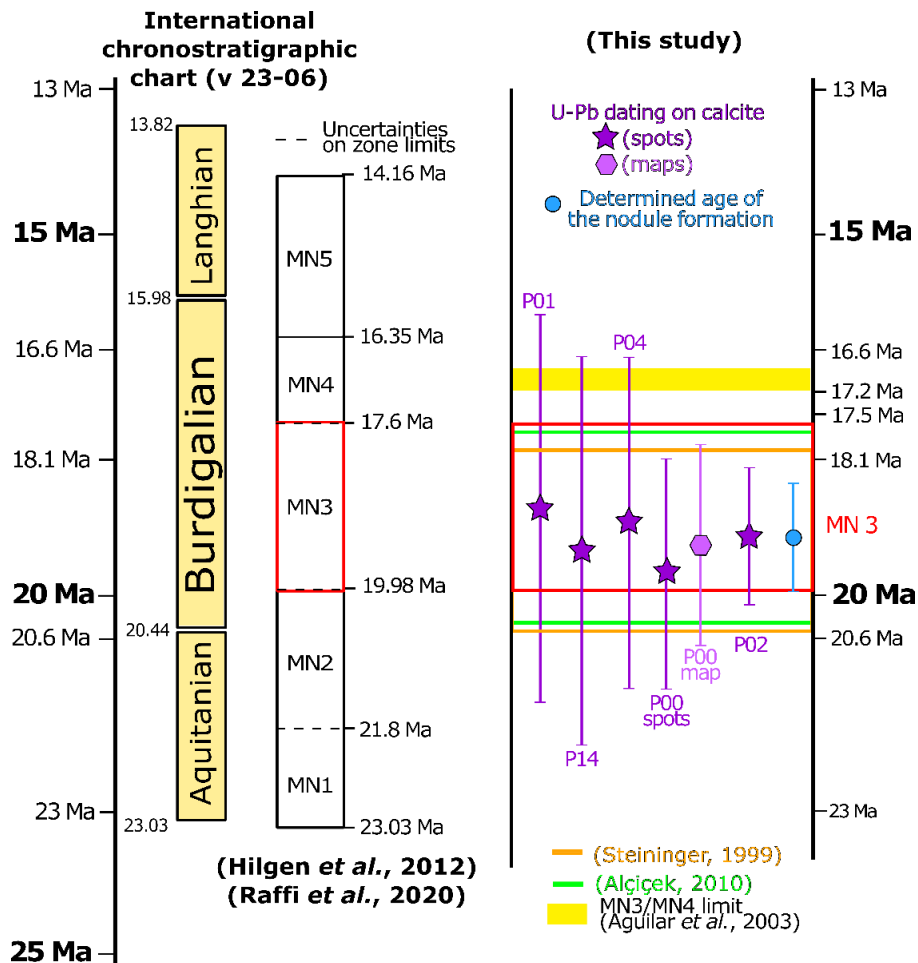
395 likely than other data to conform to a normal distribution due to the presence of outliers and the range of age values must be
396 positive, thus the distribution is asymmetric (Vermeesch, 2018). The log of the outliers used in radial plots will smooth these
397 deviations and heteroscedastic variation (unequal uncertainties) and make it fit to the normal distribution curve (Galbraith et
398 al. 1999), which is why the radial plot central age is preferred. This age of $19.22 \pm 0.66/0.79$ Ma for the s1 bed allows precise
399 correlation with other dated sequences, independently of the lithofacies or fossil assemblages present. This age is the first
400 absolute age for the continental Miocene facies of the Paris Basin and to the best of our knowledge the youngest U-Pb age
401 from pedogenic carbonates in the literature (Table 1).

402 **5.3 Biostratigraphic significance**

403 The MN (Mammal Neogene) stratigraphic timescale is based on faunal calibration. The appearance and disappearance of taxa
404 result in a given combination of species that can be linked to a given time (Mein, 1999). The MN scale incorporates a
405 stratigraphic component as well as classical stratigraphic correlations and magnetostratigraphy to help refine the age control
406 (Hilgen et al., 2012). MN units were initially defined without boundaries or clearly defined limits (e.g. Mein, 1975), but
407 nowadays the scale is often presented alongside a chronostratigraphic scale, with an absolute age associated with each biozone
408 boundary (e.g. Agustí et al., 2001; Van Dam et al., 2001; Aguilar et al., 2003; Gagnaisson et al., 2023). The absolute ages of
409 the boundaries remain debated (see the example of MN3 below) due to diachronicity and incomplete paleontological and
410 magnetostratigraphical data (Fortelius et al., 2014; Ezquerro et al., 2022). Each zone is characterised by a specific fauna found
411 at a reference locality (for Europe these are mainly in Spain, France, and Germany) that can be asynchronous by up to 1 - 2
412 Myr in the Late Miocene (Van der Meulen et al., 2012; Fortelius et al., 2014; Ezquerro et al., 2022). The majority of the MN
413 zones have uncertainties attached to their age boundaries (Figure 9), while the application of the MN timescale typically
414 involves comparison to the most proximal and well-constrained reference section to circumvent potential diachronicity. Local
415 modifications to the MN timescale are thus often adopted for selected biozones (Hilgen et al., 2012; Van der Meulen et al.,
416 2012; Fortelius et al., 2014; Ezquerro et al., 2022).

417 To improve the precision of this scale, the incorporation of magnetostratigraphy has helped to better define the MN unit
418 boundaries within basins (e.g. Agustí et al. 2001; Kälin and Kempf 2009). Steininger (1999) used magnetostratigraphic data
419 to propose that magnetochron C6r (20.5 Ma) represented the base and C5Dr the top (18.5 Ma) of MN3. The top boundary of
420 MN3 was then extended to chron C5Cn.2r, dated between 16.6 and 17.2 Ma, based on magnetostratigraphy of sections in the
421 North Alpine foreland (Agustí et al., 2001). The MN3 faunal reference site was defined as Wintershof-West with a sedimentary
422 succession dated between 17.5 and 18.5 Ma (Hilgen et al., 2012) thus only partially covering the time interval defined by the
423 magnetochron ages. The MN3 boundaries were refined by magnetochron ages for C6r (19.979 Ma) and C5Dr (18.007 – 17.634
424 Ma), which are the chrons defined by Steininger (1999) as bracketing the MN3 biozone, the ages of these magnetochrons
425 are subsequently updated by Raffi et al. (2020). It should be noted that magnetostratigraphy requires thick sections (typically
426 >10 m thick profiles) and cannot always be employed. Our results are compatible within uncertainties with the different

427 magnetochron ages proposed for MN3 and are not challenging the actual consensus around the absolute age of the base or the
 428 top of MN3 (Figure 9).
 429
 430 Absolute U-Pb dating of in-situ pedogenic carbonates enables a better understanding of the spatio-temporal distribution and
 431 evolution of continental mammalian faunas. This method is not affected by the limits detailed above (i.e. diachronicity, index
 432 fossil scarcity, insufficient profile thickness), thus offering a reliable opportunity to improve the local constraints on the MN
 433 scale. Our age is compatible with an early Orleanian stage assignation (Figure 1) and the MN3 unit (Hilgen et al. 2012). The
 434 age constraints on the Mauvières fossil locality are thus significantly improved by our results, but it should be noted that an
 435 age for one locality does not improve the precision of the MN3 boundaries at a European scale. Therefore, more studies
 436 employing similar method are needed for further improvement of the MN scale, especially zones with large uncertainties such
 as MN3.



437 Figure 9: Overview of MN timescales in the literature compared to the age data from this study. The red box defining the currently
 438 accepted boundaries of the MN3 biozone is taken from Raffi et al. (2020) by taking the base of magnetochron C6r at 19.979 Ma and
 439 the top of C5Dr as 17.634 Ma. The age of nodule formation is the result of the radial plot using the six U-Pb geochronology dates
 440 and their respective internal uncertainties; the full systematic uncertainty was propagated on to the radial plot result age calculation
 441 (see sections 4.4 and 5.2).

442 **6 Conclusions**

443 The application of LA-ICP-MS U-Pb dating of carbonate pedogenic nodules as employed in this study is a robust and reliable
444 way to provide absolute age data for terrestrial strata. Our samples yield a precise and accurate age of 19.22 ± 0.79 Ma in
445 accordance with earlier biostratigraphic estimates (Orleanian), demonstrating the suitability of the method and confirming the
446 feasibility of the technique to dating continental sedimentary facies that do not contain any index fossils or volcanic horizons
447 such as lavas or ash beds.

448 Our results are in good agreement with the biostratigraphic age (MN3 of the Neogene Mammalian timescale) of sedimentary
449 horizon s1 from Mauvières (Gagnaison et al., 2023) and represent the first absolute age constraint for the MN3 unit in France.
450 This absolute age dating approach has the potential to advance chronostratigraphy and climatic reconstructions (Liivamägi et
451 al., 2021) by improving inter-basin correlations in continental successions and extending such correlations to the marine
452 sedimentary record. In order to refine the geochronological constraints, the use of a more precise reference material would
453 decrease the external uncertainties (i.e. ASH15, Nuriel et al., 2021; JT, Guillong et al., 2020; RA138, Guillong et al., 2024).
454 The protocol for U-Pb dating of carbonate nodules proposed by Aguirre Palafox et al. (2024) offers a uniform approach and a
455 basis for comparisons between studies. While their study was published during the review process of this manuscript, it should
456 be noted that our study nevertheless broadly conforms with this protocol.

457 **Author contribution**

458 VM contributed to the conceptualisation, the formal acquisition, the investigation, the methodology, the project administration,
459 the visualisation and the writing (initial draft and edits). RR contributed to the conceptualisation, the formal acquisition, the
460 investigation, the methodology, the project administration, the visualisation and the writing (edits and part of initial draft). KD
461 contributed to the methodology, the supervision and the writing (edits). CG and BM contributed to the resources, the
462 conceptualisation and the writing (edits). RT contributed to the writing (edits). DC contributed to the supervision, the funding
463 acquisition and the writing (edits).

464 **Competing interests**

465 The authors declare that they have no conflict of interest.

466 **Acknowledgments**

467 The authors would like to acknowledge the Poirier family who allowed us to sample the shell bed (falun) in Mauvières quarry.
468 We would also like to thank Didier Memeteau and Bruno Cossard for assistance sampling the nodules. We acknowledge the
469 support of Science Foundation Ireland, the Environmental Protection Agency, and Geological Survey Ireland under

470 Investigators Programme grant 15/IA/3024. Comments by reviewers Perach Nuriel, Andreas Möller and associate editor Axel
471 Schmitt significantly improved this manuscript and are gratefully acknowledged.

472 **References**

473 Agnini, C., Fornaciari, E., Raffi, I., Catanzariti, R., Pälike, H., Backman, J., and Rio, D.: Biozonation and biochronology of
474 Paleogene calcareous nannofossils from low and middle latitudes, *Newsletter on Stratigraphy*, 47(2), 131-181.
475 <https://doi.org/10.1127/0078-0421/2014/0042>, 2014.

476 Aguilar, J. P., Antoine, P. O., Crochet, J. Y., López Martínez, N., Métais, G., Michaux, J., and Welcomme, J. L.: Les
477 mammifères du Miocène inférieur de Beaulieu (Bouchesdu-Rhône, France), comparaison avec Wintershof-West et le
478 problème de la limite MN3/MN4, *Coloquios de paleontología*, Vol. E (1), 1-24, ISSN 1132-1660, 2003.

479 Aguirre Palafox, L. E., Möller, A., McLean, N. M., Ludvigson, G. A., Colombi, C. E., and Montañez, I. P.: U-Pb
480 Geochronology of Paleosol Carbonate Cements by LA-ICP-MS: A Proof of Concept and Strategy for Dating the
481 Terrestrial Record, *Geochemistry, Geophysics, Geosystems*, 25, e2024GC011488,
482 <https://doi.org/10.1029/2024GC011488>, 2024.

483 Agustí, J., Cabrera, L., Garcés, M., Krijgsman, W., Oms, O., and Parés. J. M.: A Calibrated Mammal Scale for the Neogene
484 of Western Europe, *State of the Art. Earth-Science Reviews*, 52(4), 247-60, [https://doi.org/10.1016/S0012-8252\(00\)00025-8](https://doi.org/10.1016/S0012-8252(00)00025-8), 2001.

486 Alçıçek, H.: Stratigraphic Correlation of the Neogene Basins in Southwestern Anatolia: Regional Palaeogeographical,
487 Palaeoclimatic and Tectonic Implications, *Palaeogeography, Palaeoclimatology, Palaeoecology* 291(3), 297-318,
488 <https://doi.org/10.1016/j.palaeo.2010.03.002>, 2010.

489 Alonso-Zarza, A. M.: Palaeoenvironmental significance of palustrine carbonates and calcretes in the geological record,
490 *Earth-Science Reviews*, 60, 261-298, [https://doi.org/10.1016/S0012-8252\(02\)00106-X](https://doi.org/10.1016/S0012-8252(02)00106-X), 2003.

491 Bain, R.J., and Foos, A.M.: Carbonate microfabrics related to subaerial exposure and paleosol formation. In *Carbonate
492 Microfabrics: Frontiers in Sedimentology* (Rezak, R.; Lavoie, D.L.; editors), Springer-Verlag: 17-27, 1993.

493 Barnaby, R. J. and Rimstidt, J. D.: Redox conditions of calcite cementation interpreted from Mn and Fe contents of
494 authigenic calcites, *GSA Bulletin*, 101, 795-804, 1989.

495 Becker, M.L., Rasbury, E.T., Hanson, G.N., and Meyers, W.J.: Refinement in the age of the Carboniferous-Permian
496 boundary based on U-Pb dating of biostratigraphically constrained syn-sedimentary carbonates in the Appalachian
497 region of North America, *Newsletter on Carboniferous Stratigraphy*, 19, 18–20, 2001.

498 Boggs, S. and Krinsley, D.: Application of cathodoluminescence imaging to the study of sedimentary rocks, Cambridge
499 University Press, 2006.

500 Chew, D., Drost, K., Marsh, J. H. and Petrus, J. A.: LA-ICP-MS imaging in the geosciences and its applications to
501 geochronology, *Chemical Geology*, 559, 119917, <https://doi.org/10.1016/j.chemgeo.2020.119917>, 2021.

502 Cohen, K.M., Finney, S.C., Gibbard, P.L. and Fan, J.-X.: The ICS International Chronostratigraphic Chart, *Episodes* 36,
503 199–204, 2013; updated(09/23).

504 Daxner-Höck, G., Badamgarav, D., Barsbold, R., Bayarmaa, B., Erbajeva, M., Göhlich, U. B., Harzhauser, M., Höck, E.,
505 Höck, V., Ichinnorov, N., Khand, Y., López-Guerrero, P., Maridet, O., Neubauer, T., Oliver, A., Piller, W.,
506 Tsogtbaatar, K. and Ziegler, R.: Oligocene stratigraphy across the Eocene and Miocene boundaries in the Valley of
507 Lakes (Mongolia), *Palaeobiodiversity and Palaeoenvironments*, 97, 111–218, 2017.

508 Drake, H., Mathurin, F. A., Zack, T., Schäfer, T., Roberts, N. M. W., Whitehouse, M., Karlsson, A., Broman, C., and
509 Åström, M. E.: Incorporation of Metals into Calcite in a Deep Anoxic Granite Aquifer, *Environmental Science &*
510 *Technology*, 52, 493–502, 10.1021/acs.est.7b05258, 2018.

511 Drost, K., Chew, D., Petrus, J. A., Scholze, F., Woodhead, J. D., Schneider, J. W. and Harper, D. A. T.: An image mapping
512 approach to U-Pb LA-ICP-MS carbonate dating and applications to direct dating of carbonate sedimentation,
513 *Geochemistry, Geophysics, Geosystems*, 19, 4631–4648, <https://doi.org/10.1029/2018gc007850>, 2018.

514 Engesser, B. and Mödden, C.: A new version of the biozonation of the Lower Freshwater Molasse (Oligocene and Agenian)
515 of Switzerland and Savoy on the basis of fossil mammals. In: Aguilar, J.-P., Legendre, S. and Michaux, J., eds.
516 BiochroM'97 Montpellier, Ecole pratique des hautes études, Institut de Montpellier, Montpellier (France), 475–499,
517 1997.

518 Esteban, M., and Klappa, C. F.: Subaerial exposure environment: Chapter 1: Part 2. In: Scholle, P. A., Bebout, D.G. and
519 Moore C.H., eds. *Carbonate Depositional Environments*, 23–54, <https://doi.org/10.1306/M33429C1>, 1983.

520 Ezquerro, L., Luzón, A., Simón, J.L., and Liesa, C.L.: A review of the European Neogene Mammal zones from integration
521 of litho-, bio- and magnetostratigraphy in the Teruel Basin, *Earth-Science Reviews*, 234, 104223,
522 <https://doi.org/10.1016/j.earscirev.2022.104223>, 2022.

523 Fortelius, M., Eronen, J.T., Kaya, F., Tang, H., Raia, P., and Puolamäki, K.: Evolution of Neogene Mammals in Eurasia:
524 Environmental forcing and biotic interactions, *Annual Review of Earth and Planetary Sciences*, 42, 579-604,
525 <https://doi.org/10.1146/annurev-earth-050212-124030>, 2014.

526 Fournier, F., Montaggioni, L., and Borgomano, J.: Paleoenvironments and high-frequency cyclicity from Cenozoic South-
527 East Asian shallow-water carbonates: a case study from the Oligo-Miocene buildups of Malampaya (Offshore Palawan,
528 Philippines), *Marine and Petroleum Geology*, 21, 1-21, <https://doi.org/10.1016/j.marpetgeo.2003.11.012>, 2004.

529 Gagnaison, C.: Le Miocène du Nord-Ouest de la France (vallée de la Loire, Bretagne et Normandie) : Révision du contexte
530 taphonomique des fossiles de vertébrés, proposition d'un découpage stratigraphique et clarification des variations
531 paléoenvironnementales, *Fossiles*, 41, 3-30, 2020.

532 Gagnaison, C., Cabidoche, M., Riera, R., Dechamps, M., and Gagnaison, J.C.: The geological context of the Lower
533 Orleanian continental sands from the Savigné-sur-Lathan/Noyant-sous-le-Lude basin (Anjou-Touraine, France),
534 *Bulletin d'Information des Géologue du Bassin de Paris*, 57, 3-15, 2020.

535 Gagnaison, C., Mennecart, B., Bailleul, J., Barrier, P., Chenot, E., Toullec, R., Potel, S., Martin, H., Millet, A. and
536 Memeteau, D. : Nouvelles données géologiques et biostratigraphiques du gisement paléontologique à vertébrés de
537 Mauvières, à Marcilly-sur-Maulne (Miocène inférieur et moyen ; Indre-et-Loire, France), *Geodiversitas*, 45(16), 449-
538 478, <https://doi.org/10.5252/geodiversitas2023v45a16>, 2023.

539 Galbraith, R. F., Roberts, R.G., Laslett, R.G., Yoshida, H., and Olley, J.M.: Optical dating of single and multiple grains of
540 quartz from Jinmium rock shelter, northern Australia: part 1, experimental design and statistical models, *Archaeometry*,
541 41(2), 339-364, <https://doi.org/10.1111/j.1475-4754.1999.tb00987.x>, 1999.

542 Gates-Rector, S., and Blanton, T.: The Powder Diffraction File: A quality materials characterization database, Powder
543 Diffraction, 34(4), 352-360, <https://doi.org/10.1017/S0885715619000812>, 2019.

544 Getty, S. R., Asmerom, Y., Quinn, T. M., and Budd, A. F.: Accelerated Pleistocene coral extinctions in the Caribbean Basin
545 shown by uranium-lead (U-Pb) dating, Geology, 29(7), 639–642, <https://doi.org/10.1130/0091-7613>, 2001.

546 Ginsburg, L.: Les faunes de mammifères terrestres du Miocène moyen des Faluns du bassin de Savigné-sur-Lathan (France),
547 Geodiversitas, 23, 381-394, 2001.

548 Ginsburg L., Cheneval J., Janvier P., Pouit D. and Sen S.: Les vertébrés des sables continentaux d'âge orléanien inférieur
549 (MN3) de Mauvières à Marcilly-sur-Maulne (Indre-et-Loire), La Brosse à Meigné-le-Vicomte (Maine-et-Loire) et
550 Chitenay (Loir-et-Cher), Geodiversitas, 22(4), 597-631, 2000.

551 Guillocheau, F., Robin, C., Allemand, P., Bourquin, S., Brault, N., Dromart, G., Friedenberg, R., Garcia, J.-P., Gaulier, J.-
552 M., Gaumet, F., Grosdoy, B., Hanot, F., Le Strat, P., Mettraux, M., Nalpas, T., Prijac, C., Rigollet, C., Serrano, O., and
553 Grandjean, G.: Meso-Cenozoic geodynamic evolution of the Paris Basin: 3D stratigraphic constraints, Geodinamica
554 Acta, 13, 189-246, [https://doi.org/10.1016/S0985-3111\(00\)00118-2](https://doi.org/10.1016/S0985-3111(00)00118-2), 2000.

555 Guillong, M., Wotzlaw, J. F., Looser, N., and Laurent, O.: Evaluating the reliability of U–Pb laser ablation inductively
556 coupled plasma mass spectrometry (LA-ICP-MS) carbonate geochronology: matrix issues and a potential calcite
557 validation reference material, Geochronology, 2, 155-167, [10.5194/gchron-2-155-2020](https://doi.org/10.5194/gchron-2-155-2020), 2020.

558 Guillong, M., Samankassou, E., Müller, I. A., Szymanowski, D., Looser, N., Tavazzani, L., Merino-Tomé, Ó., Bahamonde,
559 J. R., Buret, Y., and Ovtcharova, M.: Technical note: RA138 calcite U–Pb LA-ICP-MS primary reference material,
560 Geochronology, 6, 465-474, [10.5194/gchron-6-465-2024](https://doi.org/10.5194/gchron-6-465-2024), 2024.

561 Haq, B. U., Hardenbol, J., and Vail, P. R.: Chronology of Fluctuating Sea Levels Since the Triassic, Science, 235, 1156-
562 1167, doi:10.1126/science.235.4793.1156, 1987.

563 Hilgen, F. J., Lourens, L. J., Van Dam, J. A., Beu, A. G., Boyes, A. F., Cooper, R. A., Krijgsman, W., Ogg, J. G., Piller, W.
564 E. and Wilson, D. S.: Chapter 29 - The Neogene Period. In: Gradstein, F. M., Ogg, J. G., Schmitz, M. D. and Ogg, G.
565 M. (eds.), The Geologic Time Scale, Boston, Elsevier, 2012.

566 Hoff, J.A., Jameson, J., and Hanson, G.N.: Application of Pb isotopes to the absolute timing of regional exposure events in
567 carbonate rocks; an example from U-rich dolostones from the Wahoo Formation (Pennsylvanian), Prudhoe Bay,
568 Alaska, *Journal of Sedimentary Research*, 65, 225–233, <https://doi.org/10.1306/D426807C-2B26-11D7-8648000102C1865D>, 1995.

570 Hugueney, M.: Genera Eucricetodon and Pseudocricetodon. In Rössner, G.,E., and Heissig K., (eds.), *The Miocene Land*
571 *Mammals of Europe*. Verlag Dr. Friedrich Pfeil, München: 347-358, 1999.

572 Kerr, R. A.: Huge impact tied to mass extinction, *Science*, 257, 878-880, 1992.

573 Koufos, G. D., Kostopoulos, D. S., and Vlachou, T. D.: Neogene/Quaternary mammalian migrations in eastern
574 Mediterranean, *Belgian journal of zoology*, 135, 181-190, 2005.

575 Li, Q., Parrish, R. R., Horstwood, M. S. A., and McArthur, J. M.: U–Pb dating of cements in Mesozoic ammonites:
576 *Chemical Geology*, 376, 76-83, <http://dx.doi.org/10.1016/j.chemgeo.2014.03.020>, 2014.

577 Liivamägi, S., Środoń, J., Bojanowski, M.J., Stanek, J.J., and Roberts, N.M.W.: Precambrian paleosols on the Great
578 Unconformity of the East European Craton: An 800 million year record of Baltica's climatic conditions, *Precambrian*
579 *Research*, 363, 106327, <https://doi.org/10.1016/j.precamres.2021.106327>, 2021.

580 Luczaj, J.A., and Goldstein, R.H.: Diagenesis of the Lower Permian Krider Member, Southwest Kansas, U.S.A.: Fluid-
581 Inclusion, U-Pb, and Fission-Track Evidence for Reflux Dolomitization During Latest Permian Time, *Journal of*
582 *Sedimentary Research*, 70, 762–773, <https://doi.org/10.1306/2DC40936-0E47-11D7-8643000102C1865D>, 2000.

583 Ludwig, K. R.: User's manual for Isoplot 3.75, Berkley Geochronology Center Special Publication, 5, 1–75, 2012.

584 Machel, H. G. and Burton, E. A.: Factors governing cathodoluminescence in calcite and dolomite, and their implications for
585 studies of carbonate diagenesis, in: *Luminescence Microscopy and Spectroscopy - Qualitative and quantitative*
586 *applications.*, edited by: Barker, C. E., and Kopp, O. C., Society for Sedimentary Geology, 37-57, 1991.

587 Mason, R. A.: Ion microprobe analysis of trace elements in calcite with an application to the cathodoluminescence zonation
588 of limestone cements from the Lower Carboniferous of South Wales, U.K, *Chemical Geology*, 64, 209-224,
589 [https://doi.org/10.1016/0009-2541\(87\)90003-9](https://doi.org/10.1016/0009-2541(87)90003-9), 1987.

590 Mein, P.: Report on activity RCMNS-Working groups (1971–1975), pp. 78–81, Bratislava, 1975.

591 Mein P.: European Miocene Mammal Biochronology. In Rössner, G.,E., and Heissig K., (eds.), The Miocene Land
592 Mammals of Europe. Verlag Dr. Friedrich Pfeil, München, 25-38, 1999.

593 Methner, K., Mulch, A., Fiebig, J., Wacker, U., Gerdes, A., Graham, S.A., and Chamberlain, C.P.: Rapid Middle Eocene
594 temperature change in western North America, *Earth and Planetary Science Letters*, 450, 132–139,
595 <https://doi.org/10.1016/j.epsl.2016.05.053>, 2016.

596 Monchal, V., Drost, K., and Chew, D.: Precise U-Pb dating of incremental calcite slickenfiber growth: Evidence for far-field
597 Eocene fold reactivation in Ireland, *Geology*, 51, 611-615, <https://doi.org/10.1130/G50906.1>, 2023.

598 Monchal, V., Rateau, R., Drost, K., Gagnaison, C., Mennecart, B., Toullec, R., Torremans, K., & Chew, D.: Supplementary
599 Tables : U-Pb direct dating on calcite paleosol nodules: first absolute age constraints on the Miocene continental
600 succession of the Paris Basin [Data set], Zenodo, <https://doi.org/10.5281/zenodo.14500416>.

601 Montano, D., Gasparini, M., Gerdes, A., Della Porta, G. and Albert, R.: In-situ U-Pb dating of Ries Crater lacustrine
602 carbonates (Miocene, South-West Germany): Implications for continental carbonate chronostratigraphy, *Earth and*
603 *Planetary Science Letters*, 568, 117011, 2021.

604 Nuriel, P., Weinberger, R., Kylander-Clark, A.R.C., Hacker, B.R., and Craddock, J. P.: The onset of the Dead Sea transform
605 based on calcite age-strain analyses, *Geology*, 45(7), 587-590, <https://doi.org/10.1130/G38903.1>, 2017.

606 Nuriel, P., Wotzlaw, J. F., Ovtcharova, M., Vaks, A., Stremtan, C., Šala, M., Roberts, N. M. W., and Kylander-Clark, A. R.
607 C.: The use of ASH-15 flowstone as a matrix-matched reference material for laser-ablation U – Pb geochronology of
608 calcite, *Geochronology*, 3, 35-47, [10.5194/gchron-3-35-2021](https://doi.org/10.5194/gchron-3-35-2021), 2021.

609 Pagel, M., Barbin, V., Blanc, P., and Ohnenstetter, D.: Cathodoluminescence in Geosciences: An Introduction, in:
610 Cathodoluminescence in Geosciences, edited by: Pagel, M., Barbin, V., Blanc, P., and Ohnenstetter, D., Springer Berlin
611 Heidelberg, Berlin, Heidelberg, 1-21, [10.1007/978-3-662-04086-7_1](https://doi.org/10.1007/978-3-662-04086-7_1), 2000.

612 Parrish, R. R., Parrish, C. M., and Lasalle, S.: Vein calcite dating reveals Pyrenean orogen as cause of Paleogene
613 deformation in southern England, *Journal of the Geological Society*, 175(3), 425–442, <https://doi.org/10.1144/jgs2017-107>, 2018.

615 Perry, C. T. and Taylor, K. G.: Inhibition of dissolution within shallow water carbonate sediments: impacts of terrigenous
616 sediment input on syn-depositional carbonate diagenesis, *Sedimentology*, 53, 495-513, <https://doi.org/10.1111/j.1365-3091.2006.00777.x>, 2006.

617

618 Poujol, M., Mercuzot, M., Lopez, M., Bourquin, S., Bruguier, O., Hallot, E. & Beccaletto, L.: Insights on the Permian tuff
619 beds from the Saint-Affrique Basin (Massif Central, France): an integrated geochemical and geochronological study,
620 *Comptes Rendus. Géoscience*, 355, 137-161, 2023.

621 Prajapati, N., Selzer, M., Nestler, B., Busch, B., and Hilgers, C.: Modeling fracture cementation processes in calcite
622 limestone: a phase-field study, *Geothermal Energy*, 6, 7, 10.1186/s40517-018-0093-4, 2018.

623 Prieur, M., Whittaker, A. C., Nuriel, P., Jaimes-Gutierrez, R., Garzanti, E., Roigé, M., Sømme, T. O., Schlunegger, F., and
624 Castelltort, S.: Fingerprinting enhanced floodplain reworking during the Paleocene–Eocene Thermal Maximum in the
625 Southern Pyrenees (Spain): Implications for channel dynamics and carbon burial, *Geology*, 52, 651-655,
626 10.1130/g52180.1, 2024.

627 Raffi, I., Wade, B. S., Pälike, H., Beu, A. G., Cooper, R., Crundwell, M. P., Krijgsman, W., Moore, T., Raine, I., Sardella, R.
628 and Vernyhorova, Y. V.: Chapter 29 - The Neogene Period. In: Gradstein, F. M., Ogg, J. G., Schmitz, M. D. and Ogg,
629 G. M. (eds.), *Geologic Time Scale 2020*, Elsevier, 2020.

630 Rasbury, E.T., and Cole, J.M.: Directly dating geologic events: U-Pb dating of carbonates, *Reviews of Geophysics*, 47,
631 RG3001, <https://doi.org/10.1029/2007RG000246>, 2009.

632 Rasbury, E.T., Hanson, G.N., Meyers, W.J., Holt, W.E., Goldstein, R.H., and Saller, A.H.: U-Pb dates of paleosols:
633 Constraints on late Paleozoic cycle durations and boundary ages, *Geology*, 26, 403–406, <https://doi.org/10.1130/0091-7613, 1998>.

635 Rasbury, E.T., Hanson, G.N., Meyers, W.J., and Saller, A.H.: Dating of the time of sedimentation using U-Pb ages for
636 paleosol calcite, *Geochimica et Cosmochimica Acta*, 61, 1525–1529, [https://doi.org/10.1016/S0016-7037\(97\)00043-4](https://doi.org/10.1016/S0016-7037(97)00043-4),
637 1997.

638 Rasbury, E.T., Meyers, W.J., Hanson, G.N., Goldstein, R.H., and Saller, A.H: Relationship of Uranium to Petrography of
639 Caliche Paleosols with Application to Precisely Dating the Time of Sedimentation, *Journal of Sedimentary Research*,
640 70, 604–618, <https://doi.org/10.1306/2DC4092B-0E47-11D7-8643000102C1865D>, 2000.

641 Rasbury, E. T., Piccione, G., Holt, W., and Ward, W. B.: Potential for constraining sequence stratigraphy and cycle
642 stratigraphy with U-Pb dating of carbonates, *Earth-Science Reviews*, 243, 104495,
643 <https://doi.org/10.1016/j.earscirev.2023.104495>, 2023.

644 Richter, D. K., Götte, T., Götze, J., and Neuser, R. D.: Progress in application of cathodoluminescence (CL) in sedimentary
645 petrology, *Mineralogy and Petrology*, 79, 127-166, 10.1007/s00710-003-0237-4, 2003.

646 Roberts, N. M. W. and Walker, R. J.: U-Pb geochronology of calcite-mineralized faults: Absolute timing of rift-related fault
647 events on the northeast Atlantic margin, *Geology*, 44(7), 531-534, <https://doi.org/10.1130/G37868.1>, 2016.

648 Roberts, N. M. W., Drost, K., Horstwood, M. S. A., Condon, D. J., Chew, D., Drake, H., Milodowski, A. E., McLean, N. M.,
649 Smye, A. J., Walker, R. J., Haslam, R., Hodson, K., Imber, J., Beaudoin, N., and Lee, J. K.: Laser ablation inductively
650 coupled plasma mass spectrometry (LA-ICP-MS) U–Pb carbonate geochronology: strategies, progress, and limitations,
651 *Geochronology*, 2, 33–61, <https://doi.org/10.5194/gchron-2-33-2020>, 2020.

652 Roberts, N. M. W., Žák, J., Vacek, F. and Sláma, J.: No more blind dates with calcite: Fluid-flow vs fault-slip along the
653 Očkov thrust, Prague Basin, *Geoscience Frontiers*, 12, 101143, <https://doi.org/10.1016/j.gsf.2021.101143>, 2021.

654 Roberts, N. M. W. and Holdsworth, R. E.: Timescales of faulting through calcite geochronology: A review, *Journal of
655 Structural Geology*, 158, 104578, <https://doi.org/10.1016/j.jsg.2022.104578>, 2022.

656 Smith, P. E. and Farquhar, R. M.: Direct dating of Phanerozoic sediments by the ^{238}U – ^{206}Pb method, *Nature*, 341, p. 518,
657 1989.

658 Smith, J.J., Ludvigson, G.A., Layzell, A., Möller, A., Harlow, R.H., Turner, E., Platt, B. and Petronis, M.: Discovery of
659 Paleogene deposits of the central High Plains aquifer in the western Great Plains, USA. *Journal of Sedimentary
660 Research*, 87(8), 880-896, 2017.

661 Steininger F, F.: Chronostratigraphy, geochronology and biochronology of the Miocene "European Land Mammal Mega-
662 Zones" (ELMMZ) and the Miocene "Mammal-Zones (MN-Zones)". In: Rössner, G. E. and Heissig, K. (eds.) The
663 Miocene : Land Mammals of Europe, 9-24, Friedrich Pfeil, 1999.

664 Subarkah, D., Nixon, A. L., Gilbert, S. E., Collins, A. S., Blades, M. L., Simpson, A., Lloyd, J. C., Virgo, G. M., and Farkaš,
665 J.: Double dating sedimentary sequences using new applications of in-situ laser ablation analysis, *Lithos*, 480-481,
666 107649, <https://doi.org/10.1016/j.lithos.2024.107649>, 2024.

667 Temey, I.: Le Néogène de Touraine: approche environnementale et paléogéographique des faluns du bassin de Noyant-
668 Savigné (Indre-et-Loire et Maine-et-Loire, France), Mémoire d'Ingénieur géologue, Institut Géologique Albert-de-
669 Lapparent, Cergy-Pontoise, 73, 292p, 1996.

670 Van Dam, J. A., Alcalá, L., Zarza, A. A., Calvo, J. P., Garcés, M., and Krijgsman, W.: The Upper Miocene Mammal Record
671 from the Teruel-Alfambra Region (Spain). The MN System and Continental Stage/Age Concepts Discussed, *Journal of*
672 *Vertebrate Paleontology*, 21(2), 367–385, <http://www.jstor.org/stable/20061959>, 2001.

673 Van der Meulen, A.J., García-Paredes, I., Álvarez-Sierra, M.A., Van den Hoek Ostende, L.W., Hordijk, K., Oliver, A., and
674 Peláez-Campomanes, P.: Updated Aragonian biostratigraphy: Small Mammal distribution and its implications for the
675 Miocene European Chronology, *Geologica Acta*, 10(2), 159-179, <https://doi.org/10.1344/105.000001710>, 2012.

676 Vermeesch, P.: IsoplotR: A free and open toolbox for geochronology, *Geoscience Frontiers*, 9, 1479-1493,
677 <https://doi.org/10.1016/j.gsf.2018.04.001>, 2018.

678 Wang, Z.S., Rasbury, E.T., Hanson, G.N., and Meyers, W.J.: Using the U-Pb system of calcretes to date the time of
679 sedimentation of clastic sedimentary rocks, *Geochimica et Cosmochimica Acta*, 62, 2823–2835,
680 [https://doi.org/10.1016/S0016-7037\(98\)00201-4](https://doi.org/10.1016/S0016-7037(98)00201-4), 1998.

681 Wendler, F., Okamoto, A., and Blum, P.: Phase-field modeling of epitaxial growth of polycrystalline quartz veins in
682 hydrothermal experiments, *Geofluids*, 16, 211-230, <https://doi.org/10.1111/gfl.12144>, 2016.

683 Winter, B.L., and Johnson, C.M.: U-Pb dating of a carbonate subaerial exposure event, *Earth and Planetary Science Letters*,
684 131, 177–187, [https://doi.org/10.1016/0012-821X\(95\)00026-9](https://doi.org/10.1016/0012-821X(95)00026-9), 1995.

685 Wright, V. P.: *Paleosols. Their Recognition and Interpretation*, Princeton University Press, Blackwell Scientific, Oxford,
686 1987.

687 Wright, V. P.: A micromorphological classification of fossil and recent calcic and petrocalcic microstructures. In: Douglas,
688 L. A. (eds.) *Soil Micromorphology. Proceedings of 8th meeting of Soil Micromorphology*, San Antonio, 1988 .
689 *Developments in Soil Science*, 19, Elsevier, Amsterdam, 401–407, 1990.

690 Zamanian, K., Pustovoytov, K., Kuzyakov, Y.: Pedogenic carbonates: Forms and formation processes, *Earth-Science
691 Reviews*, 157, 1-17, <http://dx.doi.org/10.1016/j.earscirev.2016.03.003>, 2016.